Equilibrium Properties of Mesoscopic Quantum Conductors

L. Saminadayar

*Université Joseph Fourier, Grenoble, France and
Centre National de la Recherche Scientifique, Grenoble, France*

C. Bäuerle

Centre National de la Recherche Scientifique Grenoble, France

D. Mailly

Centre National de la Recherche Scientifique, Marcoussis, France

CONTENTS

1. INTRODUCTION

The emergence of mesoscopic physics has led to the discovery of many striking new phenomena in solid-state physics in the last two decades [1]. This field is also intimately related to the progress in fabrication techniques: the possibility of creating objects of submicron size has allowed us to fabricate and manipulate conductors which are fully coherent.

In solid-state physics, one usually considers *macroscopic* systems. This term often refers to the notion of the thermodynamic limit: the number of particles N and the volume of the system Ω both tend to infinity, whereas the ratio $n = N/\Omega$ is kept constant [2, 3]. This idea is also closely related to the physical size of the system: the sample is considered as macroscopic as soon as its size is larger than some characteristic length, for example, the typical distance between two particles, $n^{-1/3}$. Below this size, the system is said to be *microscopic*.

It is well known from our daily experience that macroscopic objects obey classical mechanics, whereas microscopic ones are governed by quantum mechanics. This dichotomy between microscopic and macroscopic behavior is quite familiar: small particles exhibit wave-like attributes, and they must be described by quantum mechanics that allows for wave behavior like diffraction or interference. Electrons have been observed to interfere in many experiments in vacuum. However, if one considers a large number of electrons in a disordered medium, like a macroscopic piece of metal at room temperature, the conductivity is described in a classical way *via* the Boltzmann equation, which leads to the Drude formula.

The question is then: is it possible to observe the wave-like behavior of the electrons in a solid? Actually, the characteristic length which is relevant is the length over which the electronic wave keeps a well-defined phase, namely, the *phase-coherence length* l_ϕ. This phenomenon is well known in optics: incoherent light cannot give rise to interference patterns.

At room temperature, the phase-coherence length of an electron in a metal is on the order of a nanometer, roughly the $n^{-1/3}$ factor mentioned above. However, at low temperature, let us say below 1 K, this phase-coherence length increases, and may reach several micrometers in metals or

even more than 10 μm in the highest quality semiconductor heterojunctions. Combined with the progress of fabrication techniques, this allows us to observe the quantum behavior of the electrons in solids. It should be stressed that a micron size sample is, in a sense, really macroscopic when compared to microscopic scales (for example, the interatomic distances): if a mesoscopic sample behaves like a large molecule to some extent, it still contains a rather large number of atoms and electrons (more than 10^{20}). However, as the electronic wavefunction is fully coherent over the whole sample, this sample is really a *quantum conductor* [4, 5].

It is important to point out that the physics of such a system is completely different from the physics of free electrons in vacuum. First, as we said, the sample is macroscopic, and some notions, reminiscent of the standard solid-state physics, are still relevant: the Fermi wavelength, Fermi level, Fermi velocity, or chemical potential still make sense; more importantly the energy spectrum is discrete or, at least, the interlevel spacing $\Delta \approx L^{-d}$, where L is the size of the system and d is the dimensionality, may become comparable or even smaller than the temperature T. Secondly, disorder is still present in solids at the micron scale: thus, the electronic wave propagates in a random medium, and its electronic motion is still diffusive.

It is often tempting to make analogies between interference phenomena in mesoscopic physics and optics. Such a comparison may sometimes be appropriate: for example, the Young slit experiment and the Sagnac effect are very similar to some transport experiments on mesoscopic rings like the Aharonov-Bohm conductance oscillations [6, 7] or the quantization of the conductance, which may be understood in the light of the theory of waveguides [8]. There are, however, two important differences: first, electrons are fermions, and this obviously strongly affects the energy spectra of mesoscopic samples, and consequently their transport and thermodynamic properties; second, electrons are charged particles, and couple to the vector potential of the electromagnetic field. This provides a powerful tool to control interference effects simply by applying a magnetic flux.

This chapter is organized as follows: in the first part, we give the fundamental length scales which are important in mesoscopic physics. We then give an overview of the different materials commonly used in this field. In the second part, we present a comprehensive overview of the different fabrication techniques. Finally, the third part is devoted to the thermodynamics of theses mesoscopic systems.

2. MESOSCOPIC SYSTEMS

2.1. Mesoscopic Samples

2.1.1. Characteristic Lengths

Mean-free path A mesoscopic sample is a disordered sample: even at zero temperature, electrons are scattered by static defects like impurities, grain boundaries, or the edge of the sample. Such events are elastic scattering in the sense that their energy is conserved during the collision. The disorder just acts like a static, random potential which adds to the lattice potential. In such a system, Bloch states are no more eigenstates, but the system is still Hamiltonian. It

should be pointed out that the translational invariance of the crystal lattice is destroyed by such defects, but this usually does not affect the electronic properties of the system. The typical length associated with these scattering processes is l_e, often called the mean-free path. The time associated with these collisions is τ_e, and they are related via the relation $l_e = v_F \tau_e$, v_F being the Fermi velocity.

On the contrary, other collisions are inelastic in the sense that the energy of an electron is not conserved. Such processes are irreversible, and are related to the coupling of the electrons with their environment, that is, other electrons, phonons, or photons. The inelastic length is given by $l_{in} = \min\{l_{e-e}, l_{e-photon}, l_{e-phonon}\}$. At high temperature (typically above 1 K), the dominant mechanism is electron–phonon scattering. At low temperature, however, the dominant process is electron–electron scattering [2, 3].

Another important source of decoherence is electron–photon scattering. This is especially the case in micrometer size samples, where small dissipation (10^{-15} W) is sufficient to heat the conduction electrons at very low temperatures. Extreme care should therefore be taken for external radio-frequency filtering [9–11] when working in the millikelvin temperature range.

Phase-coherence time After an inelastic scattering event, the energy of the electron changes, and the phase of the wavefunction is randomly distributed between 0 and 2π; thus, the quantum coherence is lost, and the phase-coherence time is mainly limited by the inelastic time $\tau_\phi \approx \tau_{in}$. It is important to note, however, that elastic scattering also leads to dephasing: the wavevector $\vec{k}$ changes to $\vec{k}'$ after such a diffusion; elastic scattering implies only that $|\vec{k}| = |\vec{k}'|$, but there is a priori no condition on their respective directions. The point is that this dephasing is perfectly deterministic and reproducible: two successive electrons with the same wave vector $\vec{k}$ will be scattered and dephased in exactly the same way, which could be calculated if the scattering potential were known. The phase coherence is thus preserved, and interference effects are not destroyed. On the contrary, inelastic scattering depends on the state of the environment the electron interacts with at the time of the interaction. In this case, the dephasing is random, and the phase coherence is lost. This is why, at room temperature, the dominant scattering process is the electron–phonon scattering, and the phase-coherence length is very short, typically $l_\phi \approx 1$–10 nm. In the frawework of Fermi liquid theory, the available phase space at low temperature tends to zero. As a consequence, electron–electron, electron–photon, and electron–phonon couplings all tend to zero, and hence, the phase-coherence length should diverge [12]. Recent experiments, however, seem to show that this is not the case. Presently, there is still an ongoing debate concerning this point, and we will not address this issue in this chapter [13].

Finally, it is important to mention magnetic impurities. As they are static defects at low temperature, scattering by magnetic impurities is elastic as the energy of the electron is conserved. However, the electronic spin is flipped in such a collision, and the phase coherence may be lost. The exact effect of magnetic scattering on the phase coherence time, especially when entering the Kondo regime, is far from being understood [14]. In this chapter, we will not elaborate on this

point, and will consider only systems containing no magnetic impurities.

Thermal diffusion length and the Thouless energy At distances beyond the elastic mean-free path l_e, electrons propagate in a random medium. This diffusive nature of the movement is characterized by the diffusion coefficient $D = (1/d)v_F^2\tau_e = (1/d)v_F l_e$, where d is the dimensionality of the sample. To propagate over a distance L, an electron then needs a diffusion time $\tau_d = L^2/D$. In a semiclassical picture, each diffusion path l is characterized by a probability $\Psi_l = |\Psi_l|\exp(iS_l/\hbar)$, where $S_l = \int_l \vec{k}\,d\vec{l} - Et_l$, with E being the energy of the electron and t_l the diffusion time along the path l. Over the whole sample of size L, this diffusion time is then simply τ_D. If one considers an energy range larger than $2\pi\hbar/\tau_D$, the phase of the electrons in this energy range will be distributed between 0 and 2π, and interference effects will not be observable anymore. This defines the Thouless energy (or correlation energy) $E_c = h/\tau_D = hD/L^2$. When the energy range involved is larger than E_c (e.g., when $k_B T \ge E_C$), interference effects do *not* disappear; they are simply no longer observable [15]. If the size of the sample is smaller than l_e, the time for an electron to travel across the sample becomes simply L/v_F, and the Thouless energy simply expresses as $E_c = hv_F/L$.

2.1.2. Disorder Configurations

In a macroscopic sample, one usually characterizes the disorder by some characteristic length, say the elastic mean-free path l_e. Such a parameter is relevant when considering the disorder from a "global" point of view. From a mesoscopic point of view, things may be quite different: the electronic wavefunctions are fully coherent over the whole sample, and the acquired phase depends on the precise path one electron follows. Thus, the interference pattern depends on the *microscopic* disorder configuration of the sample. Moving even a single impurity drastically affects the electronic properties of the sample. That is why two samples identical from a macroscopic point of view may behave in a completely different way due to their microscopic individuality (their *fingerprints*). This phenomenon is equivalent to the speckles observed when a coherent light beam diffracts in a random medium.

2.1.3. Quantum Coherence and the Effect of Aharonov–Bohm Flux

The most important parameter that physicists can use to probe a mesoscopic sample is the magnetic flux. As an electron is a charged particle, it couples to the vector potential $\vec{A}$ (the momentum changes as $\vec{p} \to \vec{p} + e\vec{A}$ in the Hamiltonian, with e the charge of the electron) *even if the magnetic field $\vec{B}$ is zero* ($\vec{B} = \vec{\nabla} \times \vec{A} = \vec{0}$). Note, however, that as the field is zero, or at least very weak in all of the experiments,[1] the effect of the magnetic field on the trajectories of the electrons is negligible. When propagating along a path i, the wavefunction Ψ acquires a phase simply given by

---

[1] Except in the case of the quantum Hall effect, which we will not address in this chapter.

$S = \int_i(\vec{k}(\vec{r}) + e\vec{A}(\vec{r}))d\vec{r}$. The first term is simply the equivalent of the optical path, whereas the second one characterizes the quantum coupling of the charge with the magnetic flux. This shows how applying a small magnetic field can indeed control the interference pattern of a mesoscopic sample [16]. There is no equivalent of such a possibility in optics: this is a powerful way to play with the quantum, wave-like nature of the electrons.

2.2. Materials

2.2.1. Ballistic Versus Diffusive Versus Localized

The different length scales for a mesoscopic sample are the Fermi wavelength λ_F, the elastic mean-free path l_e, and the size of the sample L. The ratio between λ_F and l_e characterizes the strength of the disorder: for $\lambda_F \ll l_e$ (or, equivalently, $k_F l_e \gg 1$ or $h/\tau_e \ll E_F$), the disorder is said to be "weak," whereas for $k_F l_e \ll 1$, the disorder is said to be "strong."

Considering the ratio between these different length scales, one can distinguish different regimes for a mesoscopic sample.

Ballistic regime ($\lambda_F \ll l_e$ and $L \le l_e$) In this regime, the disorder is very weak, and the elastic mean-free path is on the order of the size of the sample. In this case, the phase coherence length is mainly limited by electron–electron collisions. The trajectories of the electrons is mainly governed by the shape of the sample, implying that the reflections at the edges of the samples are specular. In this case, transport properties as well as equilibrium properties depend on the shape of the sample. Such systems are powerful tools to probe the energy spectra of quantum billiards.

Diffusive regime ($\lambda_F \ll l_e \ll L$) In such systems, electrons experience a large number of collisions during the traversal of the sample. Their movement is rather a Brownian motion, a random walk between impurities. The phase coherence length is then given by $l_\phi = \sqrt{D\tau_\phi}$. In this regime, the exact shape of the sample does not affect its electronic properties; only its size is relevant.

Localized regime In the case of a strong disorder, Anderson has suggested that each electron is confined in a part of the sample, and cannot travel through it: its wavefunction is exponentially decreasing on a length scale ξ, and the electron is localized in a domain of size ξ^d, with d the dimensionality of the sample, and the sample becomes an insulator [17]. For $d = 3$, there is a critical value for the disorder below which the sample becomes insulating, and one observes a metal-to-insulator transition. For $d = 1$ and $d = 2$, on the other hand, electrons are localized for an arbitrary small disorder [18]. Recent experiments, however, show that there is indeed a metal-to-insulator in some two-dimensional electron gas. As both the experimental and theoretical situations are at least unclear, we will not address this topic in this chapter [19].

Two limits are then to be considered[2]: when $\xi < L$, electrons are confined in some regions of the sample, and

---

[2] Note that one always has $\xi \ge l_e$.

conduction occurs by hopping from domain to domain. On the other hand, when $\xi \succ L$, localization domains are larger than the sample: electrons are indeed localized, but they can still explore the whole sample.

2.2.2. Dimensionality

One defines the dimensionality of a sample by comparing its size with the intrinsic characteristic lengths [20]. Usually, the most relevant length scale is the Fermi wavelength. Considering a rectangular sample of sizes L_x, L_y, and L_z, with $L_x \prec L_y \prec L_z$, one has

$$\lambda_F \ll L_x \prec L_y \prec L_z: \text{3D (bulk samples)}$$

$$L_x \leq \lambda_F \ll L_y \prec L_z: \text{2D (films)}$$

$$L_x \prec L_y \leq \lambda_F \ll L_z: \text{1D (quantum wires)}$$

$$L_x \prec L_y \prec L_z \leq \lambda_F: \text{0D (quantum dots)}$$

Such a definition is certainly the most relevant from a microscopic point of view. Note, however, that when considering transport properties, and due to the quantum nature of a mesoscopic conductor, one can also define the dimensionality of a sample by comparison with the phase-coherence length:

$$l_\phi \ll L_x \prec L_y \prec L_z: \text{3D}$$

$$L_x \leq l_\phi \ll L_y \prec L_z: \text{2D}$$

$$L_x \prec L_y \leq l_\phi \ll L_z: \text{1D}$$

2.2.3. Metals

Metals have a high charge carrier density of about 10^{22} cm^{-3}. Because of this high carrier density, the Fermi wavelength is very short, in the range of the angström. Moreover, it is impossible to use gates to modulate this electron density (a too important voltage would be necessary in the case of metals). Another consequence is that the Coulomb interaction is very efficiently screened on the scale of the Thomas–Fermi vector $q_{TF} = 2\pi e^2/\rho_0$, with ρ_0 the carrier density at the Fermi level. Even if metals can be very pure from a chemical point of view, the intrinsic disorder usually makes them diffusive conductors. The elastic mean-free path l_e is on the order of 1–100 nm, and the phase coherence length l_ϕ is on the order of a micrometer.[3]

At low temperature, some metals become superconductors. This provides a new degree of freedom and a wide variety of mesoscopic effects. In particular, the superconducting state is quite different on a mesoscopic scale as compared to its macroscopic equivalent.

2.2.4. Semiconductors

Bulk semiconductors In semiconductors, the carrier densities can range practically between 10^{14} and 10^{19} cm^{-3}. Moreover, this density can be controlled using metallic gates deposited at the surface of the sample or simply by varying the doping concentration.

In the case of very pure semiconductors, for example, those obtained by molecular beam epitaxy, the elastic mean-free path is basically limited by the distance between two doping impurities. This leads easily to l_e of ≈ 100 nm, whereas l_ϕ is on the order of several micrometers. Finally, another important difference between metals and semiconductors is that, in the latter, the effective mass of the electrons, which is related to the band structure, can be very small.

Heterojunctions To reduce the dimensionality of a conductor, one may reduce the thickness of the film itself. However, it is quite difficult to obtain real two-dimensional conductors on the scale of the Fermi wavelength λ_F. An alternative way consists of playing with the band structure of two different semiconductors. Using the impressive control of growth offered by the molecular beam epitaxy, it is possible to grow two different semiconductors on top of each other, especially if their lattice parameters are matched [21]. The most common example is GaAs and GaAlAs (III–V heterostructures), but there also exist II–VI heterostructures (CdTe/HgCdTe) or even IV–IV heterostructures (SiGe).

The different band structure, mainly the energy gap and the work function,[4] causes changes in the charge transfer between the two adjacent materials in order to equalize the electrochemical potentials. Electrons are attracted to the remaining holes, and the dipole layer formed at the interface leads to the band bending at the vicinity of the interface. True two-dimensional electron (or hole) gas at the scale of λ_F can be formed using this technique [22].

The spatial separation between charge carriers and doping impurities leads to very high-mobility materials.[5] The electronic density is typically in the range of 10^{11} cm^{-2}, leading to a relatively large Fermi wavelength, on the order of 300 Å. This large Fermi wavelength allows us to create easily true 1D or 0D structures. Moreover, the use of electrostatic gates on the top of the sample allows us to deplete the 2D electron gas underneath. Using this technique, one can modulate *in-situ* and in a reversible way the shape of the 2D electron gas, allowing us to create a wide variety of quantum devices, like quantum wires or quantum dots [20]. Moreover, the edges defined by electrostatic gates are by far less rough than those produced by etching techniques.

3. SAMPLE FABRICATION TECHNIQUES

3.1. The Size to Reach

Typically, one wants to be able to tailor samples with a size smaller than 1 μm. But the smallest size is not the ultimate goal since the roughness of the edge may play an important role. In metals, the Fermi wavelength λ_F is very short, and the roughness is always much larger than the Fermi wavelength. But in semiconductor samples, where λ_F can be several tens of nanometers, the roughness can be on

---

[3] In extremely clean metals, obtained by molecular beam epitaxy (MBE), the phase-coherence length can reach ≈ 20 μm at best.

[4] For example, in GaAlAs [23, 24], the gap E_g varies linearly with the concentration of aluminum as $E_g = 1.424 + 1.247x$ at 300 K, x being the concentration in aluminum. Moreover, the mismatch in the lattice parameter does not exceed 0.3%.

[5] The highest mobility achieved in GaAs-GaAlAs heterostructures [25] is $14 \cdot 10^6$ cm$^2 \cdot$ V$^{-1} \cdot$ s^{-1}. Mobilities of $\approx 10^6$ cm$^2 \cdot$ V$^{-1} \cdot$ s^{-1} are currently achieved in this material.

the same order. In this case, one wants the edges to be defined with a precision much smaller than λ_F. As discussed in the previous paragraph, the dimensionality of the sample depends strongly on the physics involved. For interference effects, the phase-coherence length is the characteristic length which is on the order of 1 nm at low temperatures for a good metal and more than 10 μm for high-quality 2DEG. So typically, one wants to be able to fabricate samples with a width smaller than 100 nm for metal structures and a few hundred nanometers for semiconducting ones.

3.2. Nanofabrication Technique

First of all, let us recall a standard process flow. Figure 1 resumes the main steps one must follow. The starting material is the substrate, which can be the system one wants to pattern or just a flat and neutral surface used as a support. By spinning, the substrate is coated with a layer of resist.

The resist is a material sensitive to irradiation. After exposure, the resist is developed, and the exposed (nonexposed) area will be cleared off for the case of positive (negative) resist. A rich variety of processes can be done after the lithography. A commonly used process is the lift-off technique. In this case, one covers the whole patterned substrate with a metal, for instance. The resist is then completely removed by rinsing it with a strong solvent. Only the part which had been previously patterned will be covered by the metal, so one may say that we have replaced the design on the resist by a solid pattern made of metal. This metal can be just the structure wanted or can be used as a mask for a subsequent etching process. Other processes can also be used, such as ion implantation, electrochemical growth, and so on.

3.3. Optical Lithography

Optical lithography is the dominant lithography in industry. With this technique, UV light is shed through a mask, which contains the drawing information, on a resist. The
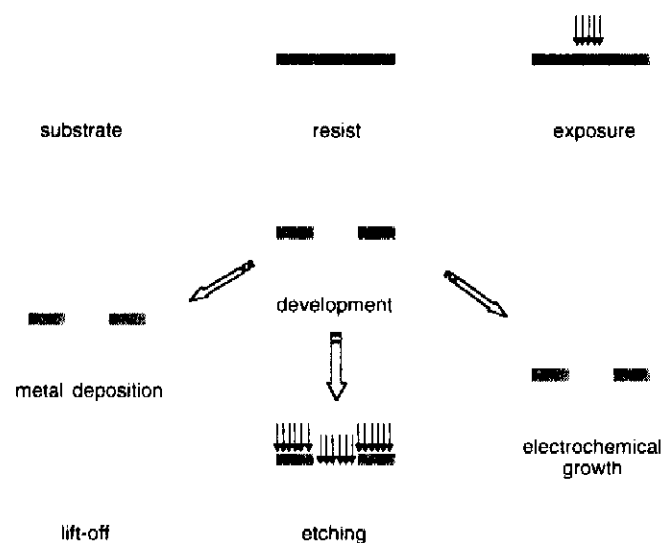

Figure 1. Typical flowchart for a fabrication process.

resolution is mostly limited by the diffraction, and hence depends on the wavelength of the light. This explains why short wavelengths are employed. Optical lithography, which started with UV (400–366 nm) is now in the DUV range (248–193 nm), and EUV (13 nm) is the next predicted range. DUV lithography can reach the sub-100 nm range, but with a complexity and costs which are too high for any scientific laboratory. For instance, the complexity of masks which use phase-shift techniques to overcome diffraction makes them difficult, and hence very expensive, to produce. Only mass production can afford such high costs. Refractive optics are presently not available in the EUV range. The fabrication of reflective optics at this wavelength is also very delicate, and it is hopeless that this technique will be inexpensive for laboratory use. Classical optical lithography, on the other hand, which uses a quartz plate mask directly pressed onto the resist with a standard DUV light, is not able to produce samples with a sub-100 nm resolution.

3.4. Electron-Beam Lithography

The possibility to finely focus an electron beam has been exploited in electron microscopy for a long time. Starting in the 1960s, focused electron beams have been used to expose a resist, and a 0.1 μm resolution was readily obtained. Ten years later, a 10 nm wide line was demonstrated using an inorganic resist. Unfortunately, this technique is essentially sequential: the electron beam is scanned pixel by pixel on the resist to draw the entire design; hence, the process is too slow to be included in an industrial processes. It is, on the other hand, the perfect technique for the laboratory. An advantage of this maskless technique is its versatility. The drawing can be easily changed on a computer with no additional cost.

In the following, we detail the electron-beam lithography to explain the resolution and limitations of this technique.

3.4.1. Resolution and Proximity Effect

Most of the resists employed in nanotechnology are polymers. The effect of the electron is to break the chain, hence leaving a polymer with a small chain, giving a better solubility. This resist is then sensitive to a very small energy compared to the one of the electron beam. Typically, one needs 10 eV to break a polymer chain, whereas for technical reasons, the focused electron beam is accelerated at several tens of kilovolts. It is then important to know how the electrons diffuse into the resist and lose their energy in order to understand how the resist is affected.

An analytical treatment is quite complex, especially in three dimensions. Monte Carlo simulations are widely used to follow the electron trajectory. Figure 2 shows electron trajectories obtained for electrons with energies of 10 and 20 kV in a silicon substrate covered with 400 nm of PMMA resist. The effects of electron diffusion are twofold. First, a forward diffusion which enlarges the spot in the resist is observed. Second, a backscattering diffusion, mainly from electrons diffused in the substrate back into the resist, but far from the initial impact of the electron, takes place. This latter effect, known as the proximity effect, has important consequences, as we will see later. The energy of the beam is quite important, as can be seen in Figure 2: higher energy
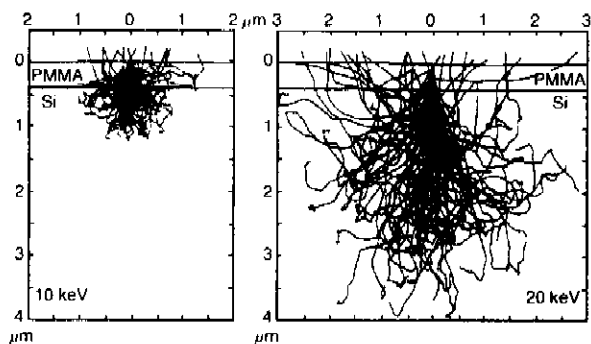
Figure 2. Monte Carlo simulation of electron trajectories in silicon substrate covered with PMMA at 10 and 20 keV. Adapted with permission from [28], D. F. Kyser and N. S. Viswanathan, *J. Vac. Sci. Technol.* 12, 1305 (1975). © 1975, Vacuum Society.

decreases the forward scattering angle and shrinks the effective beam spot. On the other hand, the electrons penetrate more deeply into the substrate as their energy increases, and are backscattered at larger distances from the impact. In other words, higher energy dilutes the proximity effect. This is the reason why recent electron-beam machines use a 100 kV source.

The total dose received by the resist at one point depends on the exposed dose at that point, but also on the vicinity around this point. Hence, a large square uniformly exposed, for instance, will be more dosed in the center than on the edge. It is also very difficult to expose two large patterns close to each other. The gap between these two patterns being exposed by proximity may result in an unwanted connection between them. Arrays of lines with a very small pitch are also very difficult. It is possible, however, to correct the dose at each point by calculating the proximity effect of the overall pattern. Softwares have been developed for that purpose, but cannot completely cure the effect of the diffusion since it may require a negative dose at certain points!

The problem of proximity effect arises from the sensitivity of organic resists to small energies. It is thus natural to try to use a resist which needs higher energy to be exposed. This is the case of an inorganic materials, for example, NaCl, AgF_2, or Al_2O_3. Such inorganic resists have been used to demonstrate the finest lines obtained by e-beam lithography, around 1 nm. The beam energy in that case gives rise to the partial or total sublimation of the resist. For instance, on AlF_3, the electron energy evaporates fluor, leaving a layer of aluminum. Hydrocarbon films have also been used where, under irradiation, a polymerization takes place. In most cases, the dose necessary to expose these types of resists is orders of magnitude higher than with a conventional resist. The total time to expose the pattern can reach nonreasonable values. Furthermore, this type of resist can be used only with thin layers which enable any lift-off process. Another possibility to avoid proximity effects is to use a very small energy. In this case, however, it is very difficult to focus the beam in conventional electron optics due to chromatic aberration. Another drawback is the forward scattering which rapidly enlarges the beam in the resist.

Figure 3 shows the best resolution obtained with different organic resists and the dose needed with e-beam lithography. One should keep in mind that the maximum current
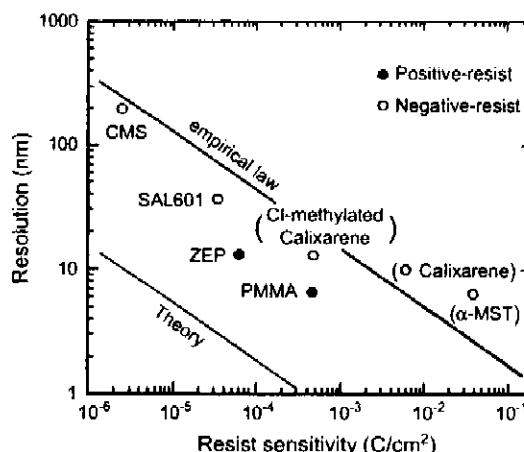

Figure 3. Resolution and sensitivity of various organic resists positive and negative for electron-beam lithography. Polymethylmetacrylate (PMMA) is presently the best organic resist, and is most widely used in scientific laboratories around the world. An example of sub-10 nm lines of PMMA with a 50 nm pitch is shown in Figure 4.

available in an e-beam system with a small spot size (less than 10 nm) is about 100 pA with a field effect gun source. This means that exposing an area of 100 μm × 100 μm at a nominal dose of 10^{-3} C/s takes more than 27 h!

An electron microscope with a computer-assisted deflection system is the basic tool for e-beam lithography. It is enough to make simple patterns in a single field. The available field size depends on the desired resolution. Lens aberrations induce severe distortions at the edge of the field which depend on the field size. With a conventional microscope, 50 μm × 50 μm is usually the maximum size one can afford to produce sub-100 nm structures. The nanostructure then has to stand within a single field since there is no possibility to displace the sample holder with enough accuracy to stitch with the previous writing field. The stability of the electron column is also a problem for long time exposure. Dedicated machines have been built to overcome the difficulties mentioned above with conventional electron microscopes. They include a laser-interferometry-controlled stage with an accuracy better than 1 nm to measure mechanical displacement. A feedback to the electron deflection is usually chosen for the field alignment. The overall field stitching accuracy is on the order of 20 nm. Using patterned marks on the sample, it is also possible to align several layers of lithography. The mark detection system combined with the laser interferometry also allows us to calibrate the deflection amplifier and to correct field distortion. It is simply done by moving a mark at different positions in the field. The exact position of the mark is known using the laser interferometry, and is compared to the position of the mark obtained by deflecting the beam. All of these essential features explain that there is at least one order of magnitude in the price of such a machine compared to a standard electron microscope.

3.5. Other Charged Particle Lithography

Focused ion beam lithography arose rapidly after electron-beam lithography as a good candidate for nanofabrication. Ions offer several advantages compared to electrons. First,
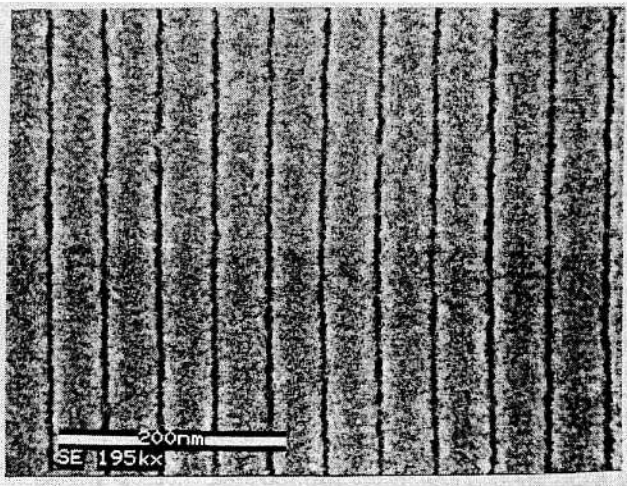
Figure 4. The image shows an example of sub-10 nm lines with a 50 nm pitch. Reprinted with permission from [26], C. Vieu et al., *Microwave Elect. Eng.* 35, 253 (1997). © 1997, American Institute of Physics.

they very quickly deliver their energy, and consequently, a much smaller dose is necessary. Second, the throughput is much better, and the proximity effect is much smaller. In addition, ions can directly erode the material, and is a resist-free process which can be very interesting for materials which are sensitive to pollution by organic materials.

In this etching mode, by varying the dose, it is also possible to produce three-dimensional structures: the paradigm of nanofabrication. Finally, at higher energy, one can locally implant atoms. On the other hand, ion lithography did not take an important place among the nanofabrication techniques. The major reason is the difficulty in producing fine spots with enough current and good stability. Recent progress in ion optics and ion source technology succeed in producing sub-10 nm spot sizes with a particle density sufficient for etching. Figure 5 shows an 8 nm line produced by such a high-resolution ion system [27].
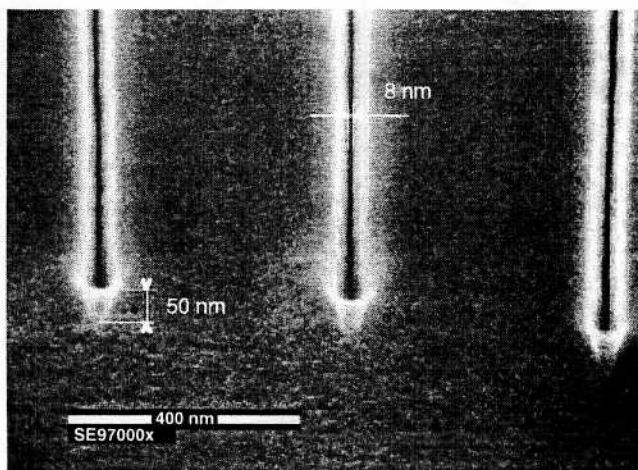

Figure 5. 8 nm line in GaAs produced using a 20 kV gallium focused ion beam. Adapted with permission from [27], J. Gierak et al., *Microwave Elect. Eng.* 57–58, 865 (2001). © 2001, American Institute of Physics.

3.6. Near-Field Techniques

Shortly after their discovery, near-field techniques have been used to produced nanostructures. The ultimate resolution has been obtained by the IBM group, who wrote the acronym of their company using Xenon atoms with a scanning tunneling microscope (STM). But such nanostructures are unfortunately very volatile. An STM can also be used in a more conventional way as a source of focused electrons. Indeed, the size of the electron spot of an STM is approximately on the order of the sample-to-tip distance, and a 10 nm spot size can readily be obtained.

Exposure of the resist is complicated by the fact that most of the resists are nonconducting. Another problem due to the proximity of the tip to the resist is the swelling of the resist under irradiation that can damage the tip. STM lithography is used more without resist by electrochemical process. For instance, it is possible to remove a group of atoms by applying a pulse on a gold surface [31]. Local oxidation is also an electrochemical process that is widely used with atomic force microscopy (AFM) lithography. The native water film on the surface of a sample at room temperature is the medium for this anodization process. In GaAlAs/GaAs samples, it is possible, for instance, to locally oxidize the surface, and the oxide formation destroys the two-dimensional electron gas beneath. Several mesoscopic structures have been produced with this technique [32]. Another example is the use of niobium, which can be anodized [33]. One of the advantages of this technique is that, using a small voltage on the tip, one can visualize the structures obtained at a higher voltage. Usually, one is limited to a small writing field because of the hysteresis of the piezodisplacement. In most cases, this technique is combined with other techniques like optical lithography. The possibility of visualization, with the AFM in the nonwriting mode, allows for the alignment of the two steps.

4. PERSISTENT CURRENTS: THEORETICAL ASPECTS

Usually, one considers *transport* properties of quantum conductors, measured by connecting voltage and current probes to the sample. In this case, however, two important properties of such a measurement must be pointed out.

- First, the strong coupling between these voltage and current probes certainly affects the quantum properties of the sample, and thus the measurement itself.
- Second, in a transport experiment, one only probes an energy range eV around the Fermi energy, with e being the electron charge and V the applied voltage. That is why one cannot access the entire energy spectrum

It is therefore very interesting to deal with the *equilibrium* properties of mesoscopic samples. It has to be stressed that such experiments in the field of mesoscopic physics are by far much more difficult than transport experiments. This is why there is only a very small number of experimental data available.

The existence of persistent currents was first suggested by London in 1937 [34], in his studies on the diamagnetism of aromatic rings (benzene rings). In 1938, Hund suggested

that such an effect could be present in clean, metallic samples at low temperature [35]. The amplitude of the persistent currents was first calculated by Bloch and Kulik in the case of a clean, 1D ring [36, 37], but their existence in a real, diffusive 3D metallic ring was only been predicted by Büttiker et al. [38] in 1983.

It is important to note that the persistent current we are considering here is a *nondissipative* current flowing in a *nonsuperconductor* ring. Another interesting point is that persistent currents and orbital magnetism are two phenomena completely equivalent from a physical point of view. Only the geometry of the sample makes one term or the other more "intuitive."

4.1. A Simple Picture: The 1D Ballistic Ring

The simplest model for the persistent currents is the case of a pure, 1D metallic ring, without disorder. Although somewhat "academic," this example allows us to present the main idea of the problem. Let us consider a ring of perimeter L pierced by a magnetic flux Φ. We take the ring to be smaller than the phase-coherence length l_ϕ, and we neglect its self-induction. The Hamiltonian for the electrons of the rings is then simply given by

$$\mathcal{H} = \frac{1}{2m}[\vec{p} - e\vec{A}]^2 + V(\vec{r}) \qquad (1)$$

where $\vec{p}$ is the momentum of the electron, e is its charge, $\vec{A}$ is the vector potential, and $V(\vec{r})$ is the periodic potential of the lattice. A simple gauge transformation $\vec{A} \Rightarrow \vec{A} + \vec{\nabla}(\int \vec{A} \cdot d\vec{l})$ leads to the Hamiltonian of free electrons $\mathcal{H}_0 = p^2/2m + V$, whereas a phase is added to the wavefunction Ψ: $\Psi(x) \Rightarrow \Psi(x)\exp(ie/\hbar \int \vec{A} \cdot d\vec{l})$. This wavefunction then obeys the new boundary conditions [39]

$$\Psi(x + L) = \Psi(x)\exp\left(i\frac{e}{\hbar}\oint \vec{A} \cdot d\vec{l}\right) = \Psi(x)\exp\left(2i\pi\frac{\Phi}{\Phi_0}\right) \qquad (2)$$

where $\Phi_0 = h/e$ is the flux quantum. These boundary conditions also lead to a new quantization for the wave vector: $k = 2\pi/L(n + \Phi/\Phi_0)$.

It should be noted that, in this case, the boundary conditions can be controlled simply by varying the magnetic flux. Moreover, such boundary conditions show that wavefunctions, eigenenergies, as well as *any thermodynamic property of the system are periodic with magnetic flux [40], with periodicity* $\Phi_0 = h/e$.

In analogy with known results on Bloch's states, one can define a velocity for each energy level [38-41]:

$$v_n = \frac{1}{\hbar}\frac{\partial \varepsilon_n}{\partial k} = \frac{L}{e}\frac{\partial \varepsilon_n}{\partial \phi} \qquad (3)$$

This velocity is equivalent to a current which is given by

$$i_n = -\frac{ev_n}{L} = -\frac{\partial \varepsilon_n}{\partial \phi} \qquad (4)$$

At zero temperature, the net current is then simply the sum of the currents carried by the N levels:

$$I_N = \sum_{n=0}^{N} i_n = \sum_{n=0}^{N} -\frac{\partial \varepsilon_n}{\partial \phi} = \frac{\partial E(N, \Phi)}{\partial \phi} \qquad (5)$$

where E is the total energy of the N electrons of the ring. However, as can be seen in Figure 6, two consecutive levels carry two currents of the same amplitude, but of opposite sign: the net current is then simply given by the last occupied level [47], that is, the Fermi level. We thus obtain for the amplitude of the persistent current

$$I_0 = \frac{ev_F}{L} \qquad (6)$$

In this expression, v_F/L is simply the time needed for an electron to perform one turn around the ring. It should be noted that this expression can be rewritten as a function of the Thouless energy hv_F/L:

$$I_0 = \frac{ev_F}{L} = \frac{hv_F}{L}\frac{e}{h} = \frac{E_c}{\phi_0} \qquad (7)$$

It should be stressed that the persistent current depends strongly on the number of electrons in the ring and on its parity, both in amplitude as well as in sign: for N
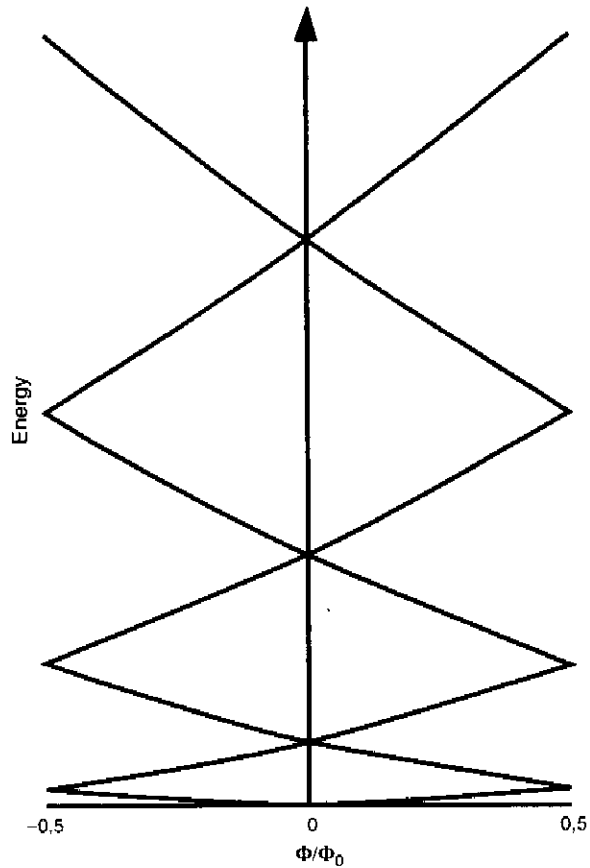

Figure 6. Energy spectrum of a pure, ballistic one-dimensional ring as a function of the magnetic flux.

even, the current is paramagnetic, whereas for N odd, it is diamagnetic.[6]

This very simple approach for the pure 1D ring allows us to give a good estimate for the order of magnitude of the persistent current. Moreover, the main features, such as the dependence on the parity of the number of electrons, remain true, even in the more realistic 3D, disordered ring.

4.2. Realistic Ring

4.2.1. Introduction

In this section, we will consider the case of diffusive, 3D rings. As we have stressed above, each sample is unique due to its specific disorder configuration. To take into account this unicity, we will consider a large number of rings, which is equivalent to averaging over disorder configurations: one obtains the *average current*. As we will see, this average current is measured in many-ring experiments. Fluctuations from this average value are also of interest, as they are accessible experimentally: this is called the *typical current*. This typical current is a good approximation of the current measured in single-ring experiments.

Another important property of the 3D case is the *spectral rigidity*. In 1D, we have seen that two successive energy levels have opposite slopes. In 3D, two successive levels repel each other: this correlation between energy levels leads to a correlation in the slopes of the energy levels [43], as can be seen in Figure 7. The slopes of two successive levels are almost identical, and this correlation extends over an energy range corresponding to the Thouless (or correlation) energy E_c. In other words, it is necessary to explore an energy range E_c to find a level of opposite slope [44, 45]. An important consequence of that is that the sign of the persistent current still depends on the number of electrons, but one has to add E_c/Δ electrons, with Δ being the mean level spacing, to reverse the sign of the persistent current [46].

4.2.2. Noninteracting Electrons

Average current The calculation of the average current [47] raises an interesting problem of statistical physics. In an experiment on many rings, the number of electrons in each ring is fixed, whereas the chemical potential μ is not. We are thus dealing with the *canonical* ensemble [48, 49]. This point is very important, as it has been shown that the persistent current calculated in the grand canonical ensemble (μ fixed) is exponentially small, $I \approx \exp(-L/2l_e)$.

On the other hand, the calculation in the canonical ensemble can be related to the calculation in the grand canonical ensemble, which is much easier to perform [1]. The canonical average persistent current is given by [50]

$$\langle I_N \rangle = -\frac{\partial \langle \mathcal{F} \rangle}{\partial \Phi}\bigg|_N = -\frac{\partial \langle \Omega \rangle}{\partial \Phi}\bigg|_\mu \qquad (8)$$

where N is the number of electrons, $\mathcal{F}$ is the free energy, Ω is the grand potential, and Φ is the magnetic flux. With μ being the sample and flux-dependent chemical potential,

---

[6] This is the case for aromatic rings: for benzene ($N = 3$), for example, the persistent current is diamagnetic.
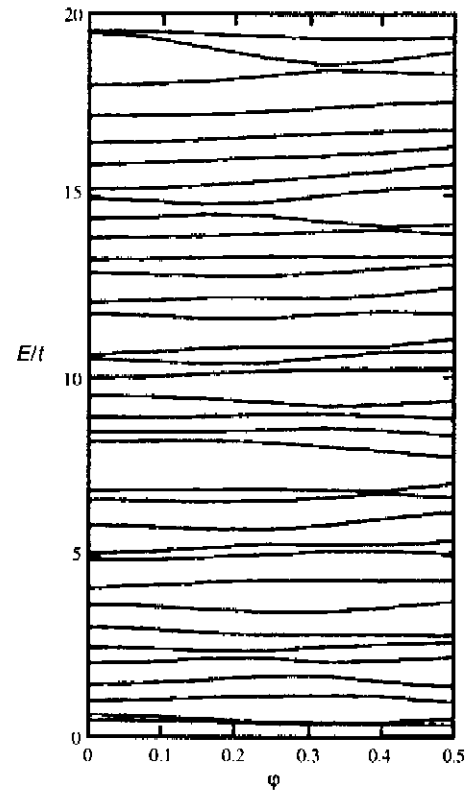
Figure 7. Energy spectrum of a real, three-dimensional diffusive ring as a function of the magnetic flux. Adapted with permission from [50], G. Montambaux, in "Quantum Fluctuations," 1996. © 1996, Elsevier Science.

one can then expand the expression (8) as a function of $\delta\mu(\phi) = \mu(\phi) - \langle\mu\rangle$, where $\langle\mu\rangle$ is flux independent:

$$-\frac{\partial\langle\Omega\rangle}{\partial\phi}\bigg|_\mu = -\frac{\partial\langle\Omega\rangle}{\partial\phi}\bigg|_{\langle\mu\rangle} - \delta\mu(\phi)\frac{\partial}{\partial\mu}\frac{\partial\langle\Omega\rangle}{\partial\phi}\bigg|_{\langle\mu\rangle} \qquad (9)$$

$$= -\frac{\partial\langle\Omega\rangle}{\partial\phi}\bigg|_{\langle\mu\rangle} - \delta\mu(\phi)\frac{\partial}{\partial\phi}\frac{\partial\langle\Omega\rangle}{\partial\mu}\bigg|_{\langle\mu\rangle} \qquad (10)$$

The first term is simply the grand canonical current, which is exponentially small, and will be neglected. The term $\partial\langle\Omega\rangle/\partial\mu$ corresponds to the number of electrons. Using the relation $\delta\mu = -\delta N \partial\mu/\partial N|_\phi$, we obtain

$$\langle I_N \rangle = -\frac{\partial\mu}{\partial N}\bigg|_\phi \left(\delta N \frac{\partial N}{\partial\phi}\bigg|_{\langle\mu\rangle}\right) \qquad (11)$$

where $\partial\mu/\partial N|_\phi$ is the level spacing. Finally, one obtains [52–55]

$$\langle I_N \rangle = -\frac{\Delta}{2}\frac{\partial}{\partial\phi}\langle\delta N_\mu^2\rangle \qquad (12)$$

The number of electrons is simply given by $N = \int_{-\epsilon_F}^0 \rho(\epsilon)d\epsilon$. The fluctuation in the number of electrons is

given by

$$\langle \delta N_\mu^2 \rangle = \langle (N - \langle N \rangle)^2 \rangle$$

$$= \left\langle \int_{-\varepsilon_F}^{0} (\rho(\varepsilon) - \rho_0) d\varepsilon \int_{-\varepsilon_F}^{0} (\rho(\varepsilon') - \rho_0) d\varepsilon' \right\rangle$$

$$= \int_{-\varepsilon_F}^{0} \int_{-\varepsilon_F}^{0} (\langle \rho(\varepsilon)\rho(\varepsilon') \rangle - \rho_0^2) d\varepsilon d\varepsilon'$$

$$= \int_{-\varepsilon_F}^{0} \int_{-\varepsilon_F}^{0} K(\varepsilon, \varepsilon') d\varepsilon d\varepsilon'$$

where $K(\varepsilon, \varepsilon')$ is the two-point correlation function of the density of states. The average current is then given by

$$\langle I_N \rangle = -\frac{\Delta}{2} \frac{\partial}{\partial \phi} \int_{-\varepsilon_F}^{0} \int_{-\varepsilon_F}^{0} K(\varepsilon, \varepsilon') d\varepsilon d\varepsilon' \qquad (13)$$

It has been shown [56] that the spectral form factor $\tilde{K}(t)$ can be related to the return probability to the origin $P(t) = P(\vec{r}, \vec{r}, t)$:

$$\tilde{K}(t) = \frac{1}{4\pi^2} t P(t) \qquad (14)$$

which leads to

$$\langle I_N \rangle = -\frac{\Delta}{4\pi^2} \frac{\partial}{\partial \phi} \int_{0}^{\infty} \frac{P(t)}{t} dt \qquad (15)$$

This return probability contains two terms: the first one is flux independent, and will be ignored. The interference term $P_{int}(t)$ can be expressed as a function of the winding number of the different trajectories m:

$$P_{int}(t) = \sum_{m=-\infty}^{\infty} P_m(t) \cos\left(4\pi m \frac{\phi}{\phi_0}\right) \qquad (16)$$

Inserting this into Eq. (15), one obtains

$$\langle I_N \rangle = \frac{2}{\pi} \frac{\Delta}{\phi_0} \sum_{m=1}^{\infty} m \sin\left(4\pi m \frac{\phi}{\phi_0}\right) \int_{0}^{\infty} \frac{P_m(t)}{t} dt \qquad (17)$$

Knowing the expression for $P_m(t)$: $P_m(t) = 1/\sqrt{4\pi Dt} \times \exp(-(m^2 L^2/4Dt))$, one finally obtains [57]

$$\langle I_N \rangle = \frac{2}{\pi} \frac{\Delta}{\phi_0} \sum_{m=1}^{+\infty} \sin\left(4\pi m \frac{\phi}{\phi_0}\right) \exp\left(-m \frac{L}{l_\phi}\right) \qquad (18)$$

This current has a periodicity of $\phi_0/2$, and is paramagnetic for small magnetic flux. It should be stressed, however, that the amplitude of this current is on the order of $\langle I_N \rangle \approx \Delta/\phi_0$. Taking a level spacing of 100 μK (for a metallic ring with a typical radius of 1 μm), one obtains a current in the range of the pA. Such a current would certainly not be measurable, and is by far much lower than the experimentally observed value.

Typical current The typical current I_{typ} is defined as the fluctuations around the average current [47]:

$$I_{typ}^2 = \langle I^2 \rangle - \langle I \rangle^2 \approx \sqrt{\langle I^2 \rangle} \qquad (19)$$

Starting from the expression for the current

$$I = -\frac{\partial \mathcal{F}}{\partial \Phi} = \frac{\partial}{\partial \phi} \int_{-\varepsilon_F}^{0} \varepsilon \rho(\varepsilon, \Phi) d\varepsilon \qquad (20)$$

one obtains

$$I_{typ}^2 \approx \langle I^2 \rangle = \frac{\partial}{\partial \Phi} \frac{\partial}{\partial \Phi'} \int_{-\varepsilon_F}^{0} \varepsilon \varepsilon' \langle \rho(\varepsilon, \Phi) \rho(\varepsilon', \Phi') \rangle d\varepsilon d\varepsilon' \qquad (21)$$

$$= \frac{\partial}{\partial \Phi} \frac{\partial}{\partial \Phi'} \int_{-\varepsilon_F}^{0} \varepsilon \varepsilon' K(\varepsilon - \varepsilon', \Phi, \Phi') d\varepsilon d\varepsilon' \qquad (22)$$

Performing a Fourier transform[7] and using again the relation (14), one obtains [50, 56]

$$I_{typ}^2 = \frac{1}{8\pi^2} \frac{1}{\phi_0^2} \int_{0}^{\infty} \frac{(t, \phi)}{t^3} dt \qquad (23)$$

where P_{int}'' denotes the second derivative of P_{int} with respect to Φ. Using Eq. (16), one finally obtains

$$I_{typ}^2 = \frac{96}{(2\pi)^2} \left(\frac{E_c}{\phi_0}\right)^2 \sum_{m=1}^{\infty} \frac{1}{m^3} \left[1 + m \frac{L}{l_\phi} + \frac{1}{3} m^2 \left(\frac{L}{l_\phi}\right)^2\right]$$

$$\times \sin^2\left(2\pi m \frac{\phi}{\phi_0}\right) \exp\left(-m \frac{L}{l_\phi}\right) \qquad (24)$$

Keeping only the first harmonic, and assuming $l_\phi \ll L$, we find for the typical current [57]

$$I_{typ} \approx \frac{\sqrt{96}}{2\pi} \frac{E_c}{\phi_0} \approx 1.56 \frac{E_c}{\phi_0} \qquad (25)$$

This current is Φ_0 periodic. It should be noted that the amplitude is again of order E_c/Φ_0. This result can be rewritten as $I_{typ} \propto E_c/\Phi_0 \propto e/\tau_D \propto e v_F/L \cdot l_e/L$, where τ_D is the diffusion time. As derived in Section 4.1, the typical current is hence simply given by the time needed for an electron to perform one turn around the ring.

Extensivity One important property of the typical current is the fact that its amplitude increases only as $\sqrt{N_R}$, where N_R is the number of rings, since the typical current is given by the *fluctuations* around the average value.

On the contrary, the average current, such as any average value, grows simply as N_R. This has been extensively studied in the case of conductance oscillations [51], but is also true for thermodynamics properties.

4.2.3. Interacting Electrons

Motivated by the first experimental observations, where a much larger amplitude of the persistent current has been obtained than theoretically predicted, electron–electron interaction has been recognized as an important contribution to the persistent current [58]. The calculation is made in the Hartree–Fock approximation, and one assumes a screened Coulomb interaction [3?], $U(\vec{r} - \vec{r}') = U_{2D} \delta(\vec{r} - \vec{r}')$, with $U_{2D} = 2\pi e^2/q_{TF}$, q_{TF} being the Thomas–Fermi wavevector. In the Hartree–Fock approximation, the total energy E reads [59]

$$E = E^0 - \frac{U}{4} \frac{\partial}{\partial \Phi} \int n^2(\vec{r}) d\vec{r} \qquad (26)$$

---

[7] We have omitted the classical part of P which does not depend on the flux.

where E^0 is the total energy for the noninteracting electrons. Given that[x] $n(\vec{r}) = 2 \int_0^\mu \rho(\vec{r}, \omega)\,d\omega$, one finds for the interaction contribution to the average current

$$\langle I_{ee} \rangle = \left\langle \frac{\partial E}{\partial \Phi} \right\rangle = -U \frac{\partial}{\partial \Phi} \int \rho(\vec{r}, \omega_1)\rho(\vec{r}, \omega_2)\,d\vec{r}\,d\omega_1\,d\omega_2 \tag{27}$$

Again, this integral can be expressed as a function of $P(t)$:

$$\langle I_{ee} \rangle = -\frac{U\phi_0}{\pi} \frac{\partial}{\partial \Phi} \int_0^\infty \frac{P(t, \Phi)}{t^2}\,dt \tag{28}$$

Indexing by m the winding number of the trajectories, one obtains finally [60]

$$\langle I_{ee} \rangle = 16 \frac{U\rho_0}{2\pi} \lambda_0 \frac{E_c}{\phi_0} \times \sum_{m=1}^{+\infty} \frac{1}{m^2}\left[1 + m\frac{L}{l_\phi}\right]$$

$$\times \sin\left(4\pi m \frac{\phi}{\phi_0}\right) \exp\left(-m\frac{L}{l_\phi}\right) \tag{29}$$

with ρ_0 being the average density of states at the Fermi level and $\lambda = U\rho_0$ the interaction coupling constant. In the simple limit $l_\phi \ll L$, and considering only the first harmonic, one finds an average current of the order E_c/Φ_0, a result obtained in the simple model of Section 4.1. It should be noted that this current is much larger than the noninteracting current calculated in Section 4.2.2. Another interesting point is that the prefactor is proportional to the interaction parameter U: this implies that the sign of the average current depends on the attractive or repulsive nature of the interaction. Finally, it should be stressed that this result is independent of the statistical ensemble: coulombian interactions locally fix the electron density [53, 58], leading to this insensitivity to the statistical ensemble. Calculations including exact coulombian interactions lead to somewhat unclear results [61–65].

We should also mention that the fluctuations of the persistent current (the typical current) are much larger than its average value (even when including the interaction term): $\sqrt{\langle I^2 \rangle} \gg \langle I \rangle$. However, the typical current for N_R rings varies as $\sqrt{N_R}$, whereas the average current varies as N_R: for few (or single)-ring experiments, the Φ_0 periodic typical current dominates, whereas for a large number of rings, the signal is dominated by the $\Phi_0/2$ periodic average current.

Finally, it should be stressed that the calculation of the typical current is made *only* for noninteracting electrons. Attempts to include coulombian interactions [66–68] are more difficult to perform and interpret.

5. EXPERIMENTAL RESULTS

5.1. Orders of Magnitude

Due to the experimental difficulty, only a few experimental studies on persistent currents are available. In the following, we give a review of these experiments. There are two distinct sets of experiments: first, the *many-ring experiments* which have been carried out on a very large number of rings, and

second, the *single-ring experiments*. Both kind of experiments have been performed on metals and semiconductor heterojunctions. More recently, experiments have been carried out on a small number of rings.

Let us recall briefly the order of magnitude for the typical and average current. The typical current, for N_R rings, is given by

$$I_{typ} = \sqrt{\langle I^2 \rangle} = \frac{\sqrt{96}}{2\pi} \frac{ev_F}{L} \frac{l_e}{L} \sqrt{N_R} \approx 1.56 \frac{ev_F}{L} \frac{l_e}{L} \sqrt{N_R} \tag{30}$$

whereas the average current is given by

$$\langle I \rangle = \frac{16}{2\pi} \lambda \frac{E_c}{\phi_0} N_R \tag{31}$$

The coupling constant λ, when taking into account all of the orders of the interactions, is typically of the order 10^{-1}. This gives, for the average current,

$$\langle I \rangle \approx 0.25 \frac{ev_F}{L} \frac{l_e}{L} N_R \tag{32}$$

The average current, even when taking into account coulombian interactions, is one order of magnitude lower than the typical current.

In a metal, the Fermi velocity is on the order of 10^7 m·s^{-1}, whereas for semiconductors, it is typically 10^5 m·s^{-1}. The elastic mean-free path in a metal is typically 20 nm, and about 10 μm in a heterojunction. For N_R rings of radius 2 μm, one obtains the following.

* For metals:

$$I_{typ} \approx 0.3 \sqrt{N_R}\,[nA] \approx 430 \sqrt{N_R}\,[\mu_B] \tag{33}$$

$$\langle I \rangle \approx 0.05 N_R\,[nA] \approx 70 N_R\,[\mu_B] \tag{34}$$

$$E_c \approx 60\,\text{mK} \tag{35}$$

* For semiconductor heterojunctions:

$$I_{typ} \approx 2 \sqrt{N_R}\,[nA] \approx 2700 \sqrt{N_R}\,[\mu_B] \tag{36}$$

$$\langle I \rangle \approx 0.5 N_R\,[nA] \approx 670 N_R\,[\mu_B] \tag{37}$$

$$E_c \approx 380\,\text{mK} \tag{38}$$

For single- or few-ring experiments, the signal is dominated by the typical current, whereas for many-ring experiments, it is the average current which is measured. However, in all cases, the signal to be measured is rather small, and such experiments are always an experimental challenge.

In all of the experiments performed up to now, the signal detected is the magnetic flux generated by the persistent currents. Basically, two different techniques have been employed. First is the dc SQUID, either a macroscopic (standard) one [69] or an on-chip micro-SQUID [70]. The second one involves an RF resonator that allows us to detect, at the same time, both the magnetic flux generated and the "conductivity" of isolated rings.

---

[x] The factor 2 takes into account the spin.

5.2. Many-Ring Experiments

In many-ring experiments, at least when the number of rings is very large, the measured physical quantity is the average current, as it grows like the number of rings. These experiments are also easier to perform, as one deals with a "macroscopic" object, and hence the detector is simpler to design.

5.2.1. Metallic Rings

The first experimental observation of the existence of persistent currents was performed by Lévy and co-workers on a network of 10^7 copper rings [71], as shown in Figure 8. In this experiment, the rings were squares of perimeter 2.2 μm, which gives $\Phi_0 \approx 130$ G,[9] and the phase-coherence length was much larger than the perimeter of the rings.

The signal is detected using a commercial dc SQUID. It is crucial to eliminate the contribution due to magnetic impurities from the signal of the rings. For that purpose, the authors used the nonlinearity of the signal coming from the persistent currents: the magnetic field is modulated at low frequency, and the signal is detected as the second and third harmonic of the magnetic response. The procedure is repeated at several values of the magnetic field.

The experimental data are reported in Figure 9. The signal displays clear oscillations as a function of the magnetic field, with periodicity $\Phi_0/2$. The amplitude of the persistent current, deduced from the magnetic response, is 0.4 nA per ring, corresponding to $3 \cdot 10^{-3} e v_F/L$ per ring. This result, although somehow larger than predicted, is in relatively good agreement with theory, taking into account electron–electron interactions.

In this experiment, the determination of the sign of the magnetic response relies on some assumptions for the data processing. In the paper, the authors stated a diamagnetic response at zero field. This result is quite surprising as it would correspond to an attractive interaction, which is quite unlikely in a metal-like copper. On the other hand, this sign has been confirmed by a recent experiment on silver rings [72].

5.2.2. Semiconductor Rings

Another experiment has been performed on a large number of rings in a semiconductor heterojunction [73] (Fig. 10). The rings were 10^5 squares of mean perimeter 8 μm (corresponding to $\Phi_0 \approx 10$ G).[10] In such semiconductor rings, the level spacing Δ is on the order of 25 mK, much higher than in metallic rings, where it is on the order of ≈ 10 μK. In this experiment, the experimental technique to detect the persistent current is somewhat different from the technique used in the experiment by Lévy et al. Instead of measuring the dc magnetic response of the rings, the authors study the ac response of the rings to an RF excitation. Using this technique, they measure the ac complex conductance of the rings, from which they deduce the persistent currents.

[9] The sample-specific parameters in this experiment were: $l_c = 20$ nm, $E_c = 80$ mK.

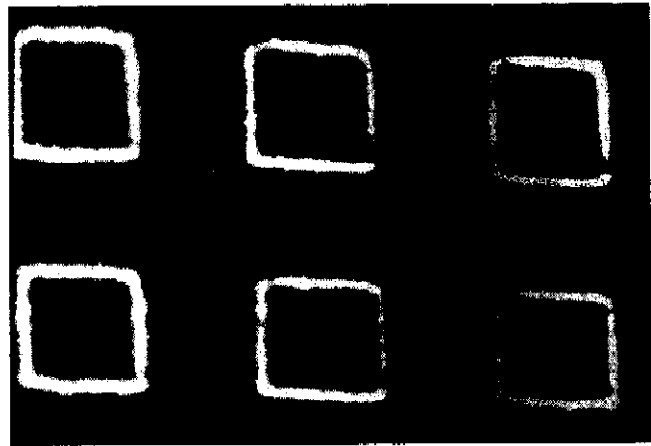[10] The sample-specific parameters in this experiment were: $l_c = 3$ μm, $E_c = 200$ mK, $l_\phi = 8$ μm.

Figure 8. Picture of a part of the sample used in the experiment of [71]. It consists of an array of 10^7 copper squares, of perimeter 2.2 μm. Adapted with permission from [71], L. P. Lévy et al., Phys. Rev. Lett. 64, 2074 (1990). © 1990, American Physical Society.

The quantity measured in this experiment is the magnetic susceptibility of the rings, $\chi(\omega) = \chi'(\omega) + i\chi''(\omega)$. The complex ac conductance of the rings is then deduced by $\chi(\omega) \propto i\omega G(\omega)$. At low frequency,[11] the imaginary part of $G(\omega)$ is just proportional to the derivative of the persistent current with respect to the flux.

The magnetic susceptibility is measured using a resonating technique. The resonator consists of a meander stripline on top of which the rings are deposited. The meander, open at both ends, is made of 20 cm of superconducting niobium. The fundamental frequency of the resonator is 380 MHz. The shift in the resonance frequency and the variations of the quality factor are proportional to the imaginary and real parts of the ac complex conductance of the rings.

The experimental conductance (see Fig. 11) shows $h/2e$ oscillations, as expected, for experiments on many rings. However, the amplitude found for the persistent current, on the order of 1.5 nA per ring, is almost an order of magnitude larger than predicted. More surprising, the measured signal implies a diamagnetic zero field persistent current, that is, an attractive interaction between the electrons. Again, such an attractive interaction is very unlikely in this two-dimensional electron gas.

It should be noted, however, that in such an experiment, the frequency is quite close to the level spacing. This may affect the response of the rings, and makes a direct comparison with the experiment by Lévy et al. somewhat difficult.

5.3. Single-Ring Experiments

Single-ring experiments are a true experimental challenge. In such experiments, it is the typical current which is detected, as it is roughly one order of magnitude larger than the average current for one ring. It should be stressed, however, that as the average current is an extensive quantity in contrast to the typical current that varies like $\sqrt{N_R}$, the signal to be detected in a many-ring experiment is orders of

[11] In this experiment, the characteristic frequency is given by the inverse of the inelastic mean free time τ_{in}^{-1}.
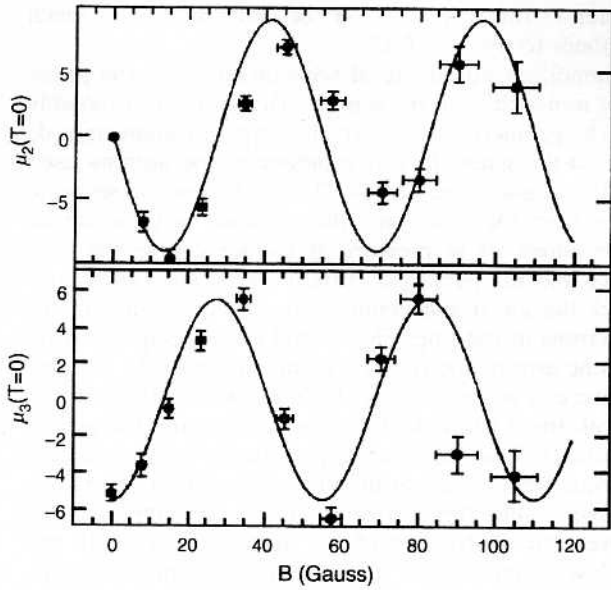
Figure 9. Dependence of the second and third harmonic of the response of the SQUID as a function of the magnetic field. In this experiment [71], Φ_0 corresponds to 130 G. Both harmonics show clear oscillations as a function of the magnetic field, with a periodicity $\Phi_0/2$. Adapted with permission from [71], L. P. Lévy et al., *Phys. Rev. Lett.* 64, 2074 (1990). © 1990, American Physical Society.
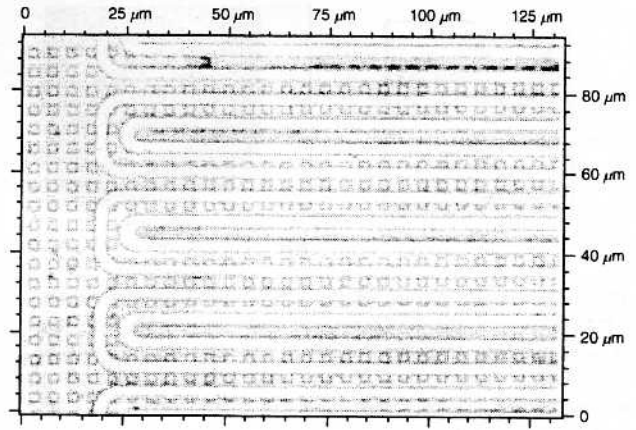

Figure 10. Optical photograph of the sample used in the experiment of [73]. It consists of an array of 10^5 GaAs/AlGaAs rings. On the top of them, one can see the niobium meander stripline used as the resonator. Reprinted with permission from [73], B. Reulet et al., *Phys. Rev. Lett.* 75, 124 (1995). © 1995, American Physical Society.

magnitude larger than the signal to be detected in a single-ring experiment.

5.3.1. Metallic Rings

The first single-ring experiment was performed by Chandrasekhar et al. [74] on a single gold ring. In this experiment, three different samples were measured: two were rings of diameter 2.4 and 4.0 μm, and the third one was a rectangle of dimensions[12] 1.4 μm × 2.6 μm.

The experimental setup consists of a homemade miniature dc SQUID. The SQUID itself has a sensitivity of $6 \cdot 10^{-8}\Phi_0$. The pick-up loop consists of a counterwound niobium loop in order to minimize the sensitivity to the static background field. To maximize the coupling between the pick-up coil and the sample, both were fabricated on the same chip, and the coil was deposited around the gold ring (see Fig. 12). Moreover, the field coil consists of a niobium line deposited around the ring.

In this experiment, the authors detect the modulation of the flux measured by the SQUID as a function of the magnetic field, which is swept over a few Φ_0. The magnetic field is modulated at low frequency ($\approx$4 Hz), and the signal is detected at f and $2f$. The background signal is subtracted numerically using a quadratic form, and the amplitude is extracted from the Fourier transform (power spectrum) of the data as a function of the magnetic field (see Fig. 13).

As a result, the authors found a persistent current with Φ_0 periodicity and an amplitude of 3 ± 2 nA, 30 ± 15 nA, and 6 ± 2 nA for the three samples investigated, whereas

the theoretical values are 0.09, 0.27, and 0.25 nA, respectively. Obviously, the measured signal is 30–150 times larger than expected. Different arguments have been invoked to explain this discrepancy. It should be noted, however, that the observed signal is on the order of ev_F/L, that is, the signal one should find for a ballistic ring ($l_e \approx L$). On the other hand, it is very unlikely that gold rings behave as ballistic rings, and the theoretical explanation of this experimental observation remains an open question.

The sign of the persistent current is quite difficult to determine in such a single-ring experiment. The authors claim that
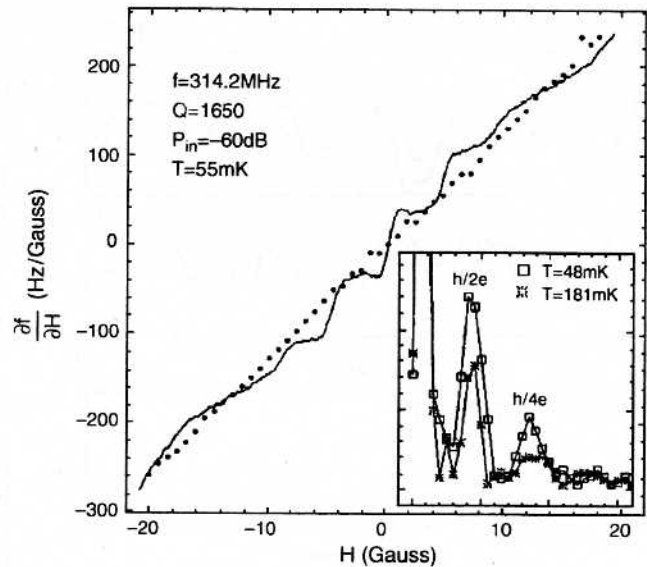

Figure 11. Derivative of the resonance frequency of the resonator used in [73]. The linear background (dotted line) is due to the diamagnetism of niobium. Superimposed on this, one clearly sees the $h/2e$ periodic signal due to the persistent currents in the rings(solid line). The inset shows the Fourier transform of the signal at two different temperatures. Reprinted with permission from [73], B. Reulet et al., *Phys. Rev. Lett.* 75, 124 (1995). © 1995, American Physical Society.
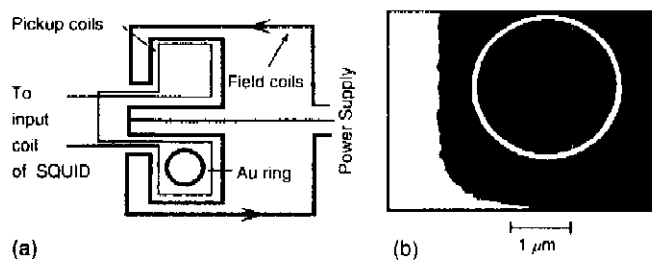
---

[12] $l_\phi = 12 \mu$m; $l_e \approx 70$ nm in this experiment.

Figure 12. (a) Schematic picture of the sample used for the experiment of [74], displaying the counterwound niobium pick-up loop, the field coil, and the gold ring. (b) Picture of the ring. The white part is a corner of the pick-up loop. Reprinted with permission from [74], V. Chandrasekhar et al., *Phys. Rev. Lett.* 67, 3578 (1991). © 1991, American Physical Society.

the samples studied showed a paramagnetic signal. A clear statement, however, as stressed by the authors, is difficult due to the few samples measured, and due to the extreme experimental difficulty.

5.3.2. Semiconductor Rings

Another experiment was performed by Mailly and co-workers on a single, isolated ring, etched into a semiconductor heterojunction [75]. In this case, the signal is expected to be larger than in metallic rings as the elastic mean-free path is much larger compared to the latter case.

The ring was etched into a two dimensional electron gas at the interface of a GaAs–GaAlAs heterojunction. The mean
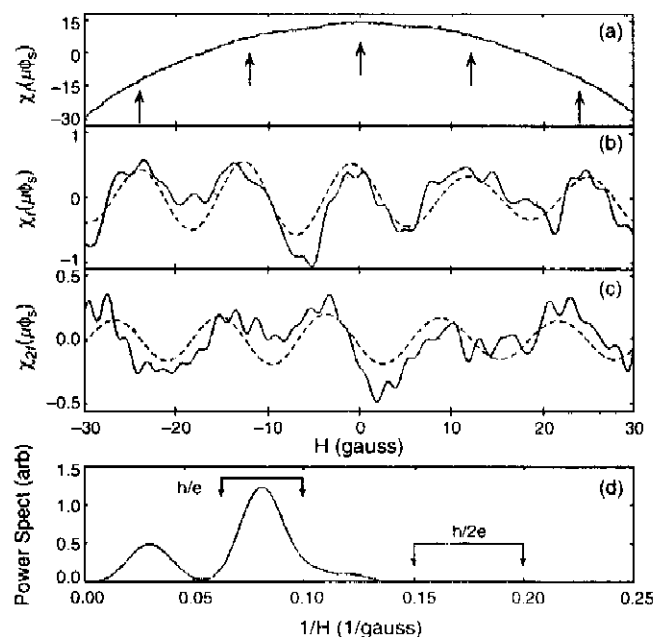

Figure 13. (a) First harmonic of the response of the dc SQUID as a function of the magnetic field. (b) Same data after subtraction of a quadratic background. (c) Second (2*f*) harmonic of the response of the dc SQUID after subtraction of a quadratic background. (d) Power spectrum of the data displayed in (b). One clearly observes a peak at h/e frequency. Reprinted with permission from [74], V. Chandrasekhar et al., *Phys. Rev. Lett.* 67, 3578 (1991). © 1991, American Physical Society.

perimeter in this sample is on the order of 6 μm, which corresponds to $\Phi_0 \approx 10$ G).[13]

An important advantage of semiconductors is the possibility of using gates on the sample. This allows us to modify *in-situ* the geometry of the sample simply by applying a dc voltage to the gates. In this experiment, the authors used two different gates (see Fig. 14). The first is used to separate the ring from the reservoirs: the presence of these ohmic contacts allows us to measure at the same time the conductance and the persistent current oscillations, and hence to check the electronic temperature and the coherence of the electrons in the ring. The second gate is evaporated on top of one arm of the ring. By polarizing this gate ("open" ring), one can suppress all of the interference effects in the ring, both the Aharonov–Bohm oscillations and the persistent currents. This allows us to perform a "zero" measurement, equivalent to measuring the SQUID with no ring. The advantage is that this can be made on the same sample. Moreover, the subtraction of the signal obtained with the ring "closed" and "open" allows us to experimentally suppress the background signal of the detector.

In this experiment, a sophisticated on-chip micro-SQUID technique was employed. With such a design, no pick-up coil is needed: the SQUID itself is deposited exactly on the top of the ring. This has two major advantages. First, the absence of a pick-up coil reduces the inductance of the setup. Second, and most important, in such a geometry, the coupling between the ring and the SQUID is basically optimal, as the SQUID has exactly the same shape as the ring. The SQUID is actually designed as a gradiometer, consisting of two counterwound loops in order to compensate the externally applied static magnetic field (see Fig. 14). The two Josephson junctions are made using Dayem microbridges, evaporated at the same time as the second level of the gradiometer. For a detailed description of the miro-SQUID gradiometer technique, we refer the reader to [76].

The measurement consists of sweeping the magnetic field over several Φ_0, and recording the critical current of the SQUID. This is made successively for the "closed" and "open" rings. The signal is then obtained by taking the Fourier transform of the difference between the two measurements. The noise is evaluated at the same time by taking the Fourier transform of the difference between two "closed" or "open" ring measurements.

In the Fourier spectrum (see Fig. 15), a clear peak is observed at the Φ_0 frequency corresponding to a value of 4 ± 2 nA for the persistent current amplitude, in good agreement with the theoretical prediction ev_F/L. No measurable signal was observed at the $\Phi_0/2$ frequency, as expected when comparing the theoretical signal and the noise level of the experiment. The sign of the persistent current, on the other hand, was impossible to determine in a reliable way.

This experiment proves that, in the case of very weak disorder and a small number of channels, standard theory gives a correct description of the persistent current amplitude. Moreover, in such samples, electron–electron interactions are much enhanced due to the low electron density. This suggests that these interactions are unlikely to strongly enhance the amplitude of the persistent currents.

---

[13] $l_e \approx 10 \mu$m, $l_\phi \approx 25 \mu$m, $E_c > 1$ K in this experiment.
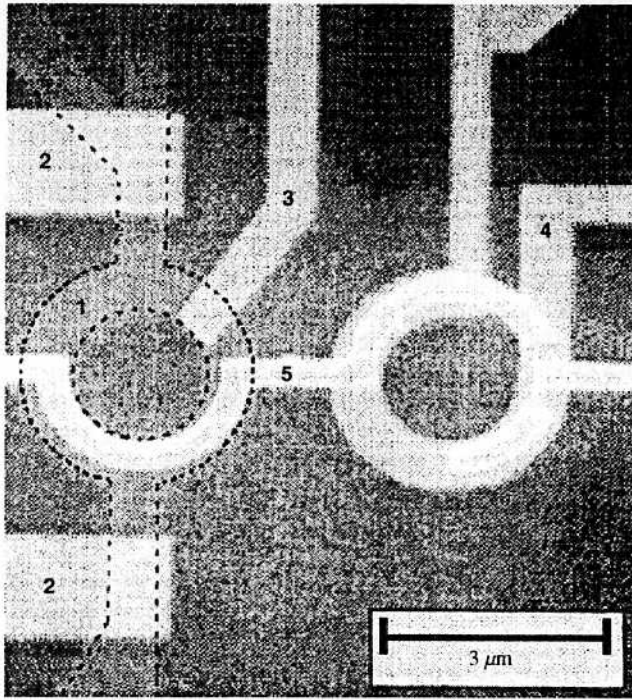
Figure 14. Picture of the sample used in [75]. 1) GaAs-GaAlAs ring (dashed line). 2), 3) gold gate used to isolate the sample from ohmic contacts and to suppress the signal. 4) Gold calibration loop. 5) First level of the micro-SQUID gradiometer containing the two Dayem microbridges on the right. The picture was taken before the evaporation of the second level of the micro-SQUID gradiometer. Reprinted with permission from [75], D. Mailly et al., *Phys. Rev. Lett.* 70, 2020 (1993). © 1993, American Physical Society.

5.4. Few-Rings Experiments

More recently, two experiments were also performed on an ensemble of a few rings, either metallic or semiconductor. In this case, the small number of rings (typically ten rings) allows us to check the theory concerning the ensemble
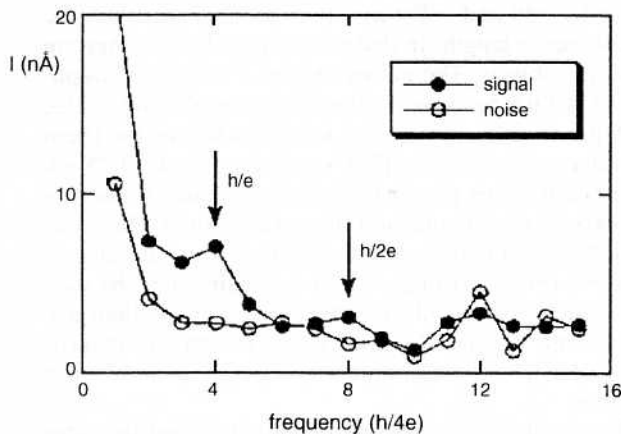

Figure 15. Fourier spectrum of the magnetization of the ring of [75] in units of nanoamperes. The arrows indicate the h/e and $h/2e$ frequency. Open dot is the experimental noise. One clearly observes the signal at the h/e frequency corresponding to a persistent current of 4 ± 2 nA in the ring. Reprinted with permission from [75], D. Mailly et al., *Phys. Rev. Lett.* 70, 2020 (1993). © 1993,

averaging, and should allow us to observe both the h/e and $h/2e$ components of the persistent current. Moreover, in the experiment on semiconductor rings, the authors were able to check the effect of a connection (ohmic contacts) between the rings.

5.4.1. Metallic Rings

In this experiment, Jariwala et al. [77] used a similar experimental setup as for the experiment on the single gold ring. The sample (see Fig. 16) consists of a line of 30 isolated gold rings of radius 1.3 μm (perimeter 8 μm) corresponding to a flux period[14] of $\Phi_0 \approx 8$ G.

To extract the persistent current signal from the background signal, the magnetic field is modulated at low frequency (typically ≈ 2 Hz), and detected at the first, second, and third harmonics of the response of the SQUID.

In this experiment, both the h/e and $h/2e$ components were detected (see Fig. 17). For the h/e component, the authors found a current of $I_{typ} = 0.35$ nA $= 2.3 E_c/\Phi_0$ per ring, in good agreement with theoretical predictions, taking into account e–e interactions. To obtain this result, the authors divided the total signal by $\sqrt{N_R}$ to account for the random sign of the persistent current. This suggests that the amplitude of the persistent current measured in the single-ring experiment [74] is somewhat overestimated.

The $h/2e$ component was found to be $\langle I_N \rangle = 0.06$ nA per ring, corresponding to $0.44 E_c/\Phi_0$. This result is in line with the results found in the previous experiment of Lévy et al. on copper rings, and only a factor of 2 larger than the theoretical predictions when taking into account electron–electron interactions.

The sign of the persistent current, on the other hand, is much more surprising. In this experiment, the sign of the average current is *diamagnetic*. Although this has been seen in previous experiments on many rings [71, 72], in this work, the determination of the sign is unambiguous. As we have seen, such a diamagnetic response is quite unlikely as it corresponds to an *attractive* interaction between the electrons. Clearly, such a discrepancy between experiment and theory may be attributed to an unexplored physical phenomenon that modifies the ground state of the electron gas. The authors of this experiment explain their result in light of a recent theory on zero temperature dephasing in metals [84]. However, as the status of such theories is still quite controversial, we will not go further into this point.

Finally, it should be noted that, in such an experiment on 30 rings, both the average current, that grows like N_R, and the typical current, that grows like $\sqrt{N_R}$, have the same amplitude. This proves that 30 rings are not enough for ensemble averaging, and the exact variation of I_{typ} and $\langle I_N \rangle$ with the number of rings remains experimentally an open question.

5.4.2. Semiconductor Rings

Another experiment was performed on a small number of semiconductor rings by Rabaud and co-workers [78]. This experiment was performed on two arrays of 4 and 16 rings (actually squares) etched into a two-dimensional electron

---

[14] $l_e \approx 87$ nm, $l_\phi \approx 16$ μm, $E_c \approx 7$ mK in this experiment.
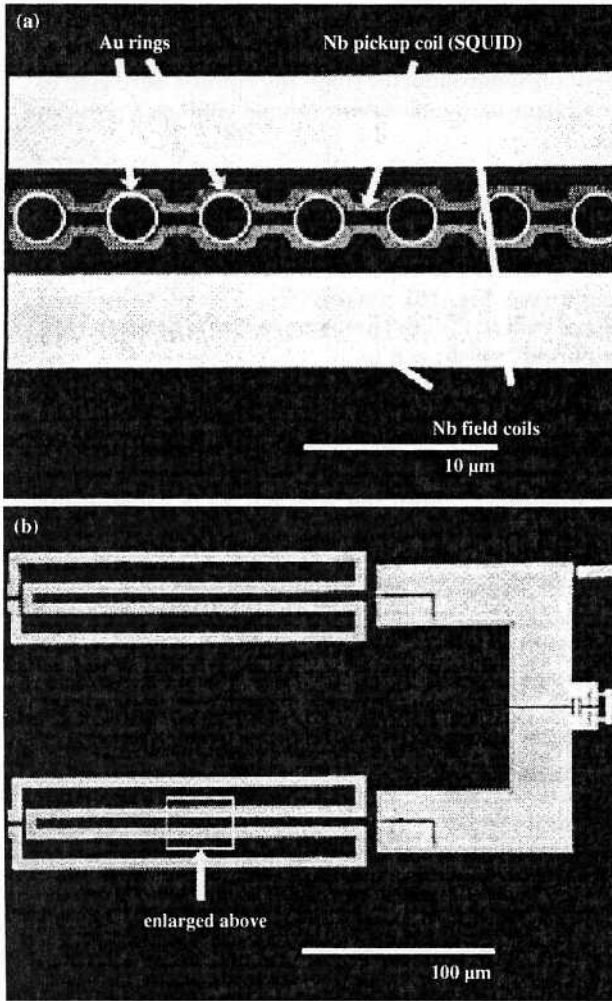
Figure 16. Picture of the sample used in the experiment of [77]. (a) Close-up view showing the gold rings, the niobium pick-up coil, and the niobium field coil. (b) Larger view showing the entire gradiometer. Reprinted with permission from [77], E. M. Q. Jariwala et al., *Phys. Rev. Lett.* 86, 1594, (2000). © 2000, American Physical Society.
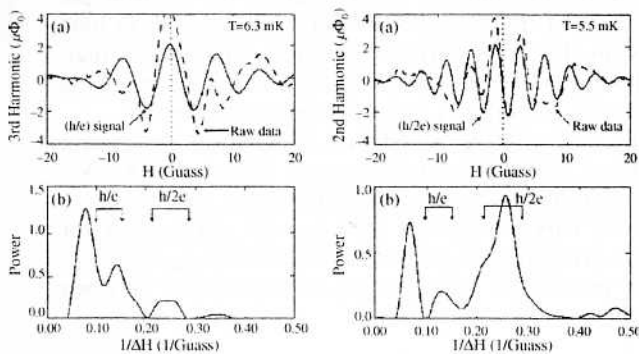

Figure 17. Magnetic response of the array of 30 gold rings of the experiment of [77]. Left panel: (a) raw data (dashed line) and h/e contribution (solid line) extracted from the Fourier spectrum displayed in (b). Right panel: (a) raw data (dashed line) and $h/2e$ contribution (solid line) extracted from the Fourier spectrum displayed in (b). Reprinted with permission from [77], E. M. Q. Jariwala et al., *Phys. Rev. Lett.* 86, 1594 (2000). © 2000, American Physical Society.

gas at the interface of a GaAs GaAlAs heterojunction. The squares were 3 μm × 3 μm, perimeter 12 μm, corresponding to $\Phi_0 \approx 5$ G).[15] Using an original setup containing three different metallic gates (see Fig. 18), Rabaud et al. were able to measure in the same experiment (same cooling down run) both the signal of connected and isolated rings. This original setup also permits us to suppress the signal via a gate, and check the "zero" of the detector. This allows us to perform an *in-situ* subtraction of the background. Such a technique has the advantage of measuring at the same time both the signal and the noise in order to have an unambiguous determination of the magnetic signal.

In this experiment, the authors measured a clear h/e periodic signal, of amplitude 2.0 ± 0.3 nA per ring for the 4-ring sample, and 0.35 ± 0.07 nA per ring for the 16-ring sample (see Fig. 19), to be compared with the theoretical values 2.18 nA per ring for the 4-ring sample and 1.09 nA per ring for the 16-ring sample. The experimental results are in relatively good agreement with the theoretical values. The discrepancy observed for the 16-ring sample may be attributed to an overestimation of the elastic mean-free path, which is determined on wires fabricated from the same wafer of the GaAs/AlGaAs heterojunction. However, the complete lithographic process, quite complicated in this experiment, may affect l_e, mainly because of the roughness of the edges after etching.

In this work, the authors were also able to measure the persistent currents in the same array of rings, but this time with an ohmic connection between the rings. Measurements on both isolated and connected rings can be made basically at the same time, by simply applying a dc voltage on the gates on the top of the arms connecting the rings. The purpose of this experiment was to measure the persistent current in a sample much larger than l_ϕ, that is, a macroscopic sample from the quantum physic point of view. This work was stimulated by theoretical models that calculated persistent currents in arrays of rings, showing that they do not vanish, but are only reduced by some geometrical factor [79].

The lines of 4 and 16 rings used in the experiment were, respectively, ≈ 60 and ≈ 250 μm, both much larger than the phase-coherence length. In that sense, these line of rings are macroscopic objects. The authors found a current of amplitude 1.7 ± 0.3 nA per ring for the 4-ring sample, and 0.40 ± 0.08 nA per ring for the 16-ring sample, whereas the theoretical values, calculated in [79], were respectively, 1.25 nA per ring and 0.62 nA per ring. There is obviously a discrepancy between experimental and theoretical values. However, it should be noted that the theoretical model was developed for diffusive (metallic) rings, which is certainly not the case in heterojunction rings. Moreover, coulomb interactions are not taken into account for the typical current; in heterojunctions, the low electronic density strongly enhances the interactions.

The key result of this experiment is the fact that the ratio between the amplitude of the persistent currents observed in connected and isolated rings is on the order of 1 for both samples. This shows that persistent currents are basically

---

[15] $l_e \approx 10$ μm; $l_\phi \approx 25$ μm; $E_c \approx 500$ mK in this experiment
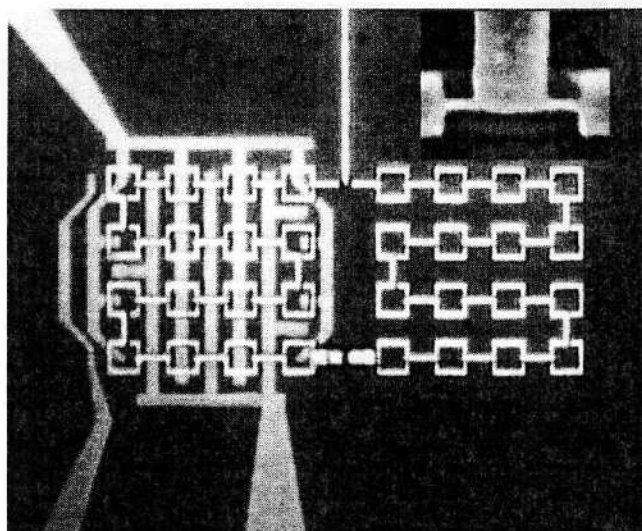
Figure 18. Optical photograph of the sample used for the experiment of [78]. The three metallic gates and the aluminum micro-SQUID gradiometer are clearly visible. Inset shows a SEM picture of the two Dayem microbridges used as Josephson junctions for the SQUID. Adapted with permission from [78], W. Rabaud et al., *Phys. Rev. Lett.* 86, 3124 (2001). © 2001, American Physical Society.

unaffected by the connection between the rings. This suggests that, even in a macroscopic sample, there should be a reminiscence of the quantum nature of electrons.

Finally, it is interesting to compare this experiment with the experiment performed on 30 metallic rings. In the experiment on semiconductor rings, no observable signal was detected at the $h/2e$ frequency for both samples. At least for the 16-ring sample, this result is quite surprising, as the average current grows linearly with the number of rings. As

Figure 19. Power spectrum of the magnetization due to the persistent current in a line of 16 connected rings in units of nanoamperes per ring. The arrow indicates the h/e frequency window. Open symbols are the experimental noise. One clearly sees a peak in in the "signal" curve, absent from the "noise" curve. Inset shows the raw data (dashed line) after substraction of the background and after bandpassing the signal over the h/e frequency range (solid line). Adapted with permission from [78], W. Rabaud et al. *Phys. Rev. Lett.* 86, 3124 (2001). © 2001, American Physical Society.

a comparison, in the experiment on metallic rings, the signals at h/e and $h/2e$ for 30 rings were of similar amplitude. Again, this shows that the ensemble averaging, in the case of persistent currents, is still not fully understood.

6. CONCLUSION

Persistent currents are certainly one of the most spectacular manifestations of the quantum coherence of the electrons in a mesoscopic system: it manifests as a permanent, nondissipative current flowing around a normal, nonsuperconducting ring. The amplitude of this current is on the order of a nanoampere, whereas the resistance of the ring can be on the order of a kilohm, for example, for the case of semiconductor rings.

Although heavily controversial at the beginning, the existence of such currents is well established, from both a theoretical as well as an experimental point of view. However, many questions remain open, and experimental results point out the lack of a deep understanding of this phenomenon.

First, the amplitude experimentally observed seems different from the theoretical predictions. Most of the experimental results are about an order of magnitude larger than the theoretical predictions. However, it must be stressed that all of these experiments are very difficult, as they deal with the measurement of very small magnetic signals. From this point of view, and taking into account the different approximations in the theoretical models, it seems difficult in the absence of new experimental results to draw a definitive conclusion concerning the validity of the theoretical predictions on the amplitude of the persistent currents.

More surprising is the sign observed in the many-ring experiments. As we have seen, the sign of the zero-field magnetic response due to the average persistent currents are directly related to the sign of the interaction between electrons. In at least two experiments on many rings, both metallic or semiconductor, the sign was found to be diamagnetic, whereas in the first experiment on copper rings, there were indications that it was also diamagnetic. This result is quite intriguing, as it should correspond to an attractive interaction between electrons. Such an attractive interaction is very unlikely in "standard" metals like copper or gold, or even in GaAs-GaAlAs heteronjunctions. Clearly, there are many open questions in the description of the average persistent current of interacting electrons.

Another interesting point is the change of persistent currents when the sample evolves from a true mesoscopic sample to a macroscopic sample. Only one such experiment has been carried out up to now, and the result found is that persistent currents are not significantly modified when the size of the sample increases. These results suggest that persistent currents should be observable in a macroscopic objet; by extension, in the spirit of the evolution from Aharonov-Bohm oscillations to weak localization, one may think about observing the zero-field magnetic response of a standard two-dimensional metal.

Finally, there are natural extensions of this problem of equilibrium properties of mesoscopic conductors that have been largely unexplored. An interesting problem is a ballistic dot of different shape, that is, quantum billiards. In this case, the properties of the energy spectrum are no longer
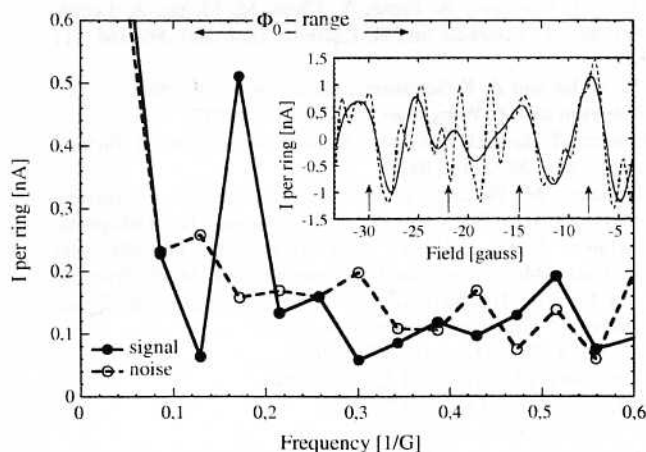
given by the impurity configuration, but by the specular scattering at the boundaries of the sample [80–82]. The orbital magnetism of these systems should be controlled by the regular or chaotic nature of the billiard, and must be understood in light of the quantum chaos theory. Another point is the connection between the persistent currents and the zero temperature decoherence: it has been proposed that the anomalously high amplitude of the average current may be related to the decoherence of the electron due to the RF environment [83, 84]. It should also be interesting to study thermodynamic properties different from the persistent current. One example is the specific heat of mesoscopic samples. In an equivalent way to persistent currents, the specific heat should oscillate with the magnetic flux. However, such a measurement is certainly very difficult, as the energy involved in such a phenomenon is again on the order of the Thouless energy. Such an experiment would imply strong improvements in the sensitivity of present detectors. Finally, one subject of major interest at present is the possibility of observing the Kondo effect in artificial nanostructures [85]. Coupling this with a persistent current measurement should allow us to directly probe the reality and the extension of the Kondo cloud [86–88].

GLOSSARY

Aharonov–Bohm flux Additional dephasing of an electronic wavefunction due to the coupling between the electric charge of the electron and the vector potential.

Ballistic conductor Conductor pure enough to allow the electrons to be scattered only by the edge of the sample.

Equilibrium (thermodynamic) property Property related to the ground state of a system.

Mesoscopic (quantum) conductor Conductor whose size is between the microscopic scale (atoms and molecules) and the macroscopic scale (daily objects).

Molecular beam epitaxy Technique used to grow semiconductors with a very high purity. This technique allows the control of atomic layer growth.

Nanolithography Technique used to fabricate samples at the nanometer scale. This includes, UV lithography, e-beam lithography, X-rays lithography etc.

Quantum coherence length Length over which the associated wave of an electron maintains a well defined phase. Beyond this length scale, the electron looses its quantum, wave-like nature.

Transport property Property related to the response of a conductor to an external excitation, e.g. the current in response to a given voltage.

REFERENCES

1. Y. Imry, "Introduction to Mesoscopic Physics." Oxford University Press, 1997.
2. N. W. Ashcroft and N. D. Mermin, "Solid State Physics." Saunders College, 1976.
3. C. Kittel, "Introduction to Solid State Physics, 6th ed." Wiley, 1986.
4. R. Landauer, *IBM J. Res. Dev.* 1, 223 (1957).
5. R. Landauer, *Philos. Mag.* 21, 863 (1970).
6. D. Y. Sharvin and Y. V. Sharvin, 34, 272 (1981).

7. R. A. Webb, S. Washburn, C. P. Umbach, and R. B. Laibowitz, *Phys. Rev. Lett.* 54, 2696 (1985).
8. B. J. van Wees, H. van Houten, C. W. J. Beenakker, J. G. Williamson, L. P. Kouwenhouven, D. van der Marel, and C. T. Foxon, *Phys. Rev. Lett.* 60, 848 (1988).
9. A. B. Zorin, *Rev. Sci. Instrum.* 66, 4296 (1995).
10. D. Vion, P. F. Orfila, P. Joyez, D. Esteve, and M. H. Devoret, *J. Appl. Phys.* 77, 2519 (1995).
11. D. C. Glattli, P. Jacques, A. Kumar, P. Pari, and L. Saminadayar, *J. Appl. Phys.* 81, 7350 (1997).
12. B. L. Altshuler and A. G. Aronov, in "Electron-Electron Interactions in Disordered Conductors" (A. L. Efros and M. Pollak, Eds.). North Holland, Amsterdam, 1985.
13. P. Mohanty, E. M. Q. Jariwala, and R. A. Webb, *Phys. Rev. Lett.* 78, 3366 (1997).
14. F. Schopfer, C. Bäuerle, W. Rabaud, and L. Saminadayar, *Phys. Rev. Lett.* 90, 056801 (2003).
15. J. Edwards and D. Thouless, *J. Phys. C* 5, 807 (1972).
16. S. Chakravarty and A. Schmid, *Phys. Rep.* 140, 193 (1986).
17. P. W. Anderson, 109, 1492 (1958).
18. E. Abrahams, P. W. Anderson, D. C. Licciardello, and T. V. Ramakrishna, *Phys. Rev.* 42, 673 (1979).
19. V. M. Pudalov, M. D'Iorio, S. V. Kravchenko, and J. W. Campbell, *Phys. Rev.* 70, 1866 (1993).
20. C. W. J. Beenaker and H. van Houten, 44, 1 (1991).
21. L. Esaki and R. Tsu, Internal Report RC 2418, IBM Research, March 1969.
22. T. Ando, A. B. Fowler, and F. Stern, *Rev. Mod. Phys.* 54, 437 (1982).
23. J. Blackmore, *J. Appl. Phys.* 53, R123 (1982).
24. S. Adachi, *J. Appl. Phys.* 58, R1 (1985).
25. V. Umansky, R. de Picciotto, and M. Heiblum, *Appl. Phys. Lett.* 71, 683 (1997).
26. C. Vieu, M. Meijas, F. Carcenac, G. Faini, and H. Launois, *Microwave Elect. Eng.* 35, 253 (1997).
27. J. Gierak, D. Mailly, G. Faini, J. L. Pelouard, P. Denk, J. Y. Marzin, A. Septier, G. Schmid, J. Ferré, R. Hydman, C. Chappert, J. Fliestein, B. Gayral, and J. M. Gerard, *Microwave Elect. Eng.* 57–58, 865 (2001).
28. D. F. Kyser and N. S. Viswanathan, *J. Vac. Sci. Technol.* 12, 1305 (1975).
29. C. Vieu, F. Carcenac, A. Pépin, Y. Chen, M. Méjias, A. Leibib, L. Ferlazzo, L. Couraud, and H. Launois, *Appl. Surf. Sci.* 164, 111 (2000).
30. D. M. Eigler and A. K. Schweizer, *Nature* 344, 524 (1990).
31. C. Lebreton and Z. Wang, *Surf. Sci.* 382, 193 (1997).
32. S. Lüscher, T. Heinzel, K. Ensslin, W. Wegscheider, and M. Bichler, *Phys. Rev. Lett.* 86, 2118 (2001).
33. V. Bouchiat, M. Faucher, T. Fournier, B. Pannetier, C. Thirion, W. Wernsdorfer, N. Clement, D. Tonneau, H. Dallaporta, S. Safarov, J. C. Villégier, D. Fraboulet, D. Mariolle, and J. Gauthier, "Micro- and Nano-engineering 2001, MNE: Proceedings of the 27th International Conference on Micro- and Nano-Engineering," Grenoble, France, Sept. 2001.
34. F. London, *J. Phys. (France)* 8, 379 (1937).
35. F. Hund, *Ann. Phys. (Leipzig)* 32, 102 (1938).
36. F. Bloch, *Phys. Rev.* 137, A 787 (1965).
37. I. O. Kulik, *JETP* 31, 1172 (1970).
38. M. Büttiker, Y. Imry, and R. Landauer, *Phys. Lett.* 96A, 365 (1983).
39. N. Byers and C. N. Yang, *Phys. Rev. Lett.* 7, 46 (1961).
40. H. F. Cheung, Y. Gefen, E. K. Riedel, and W.-H. Shih, *Phys. Rev. B* 37, 6050 (1988).
41. R. Landauer and M. Büttiker, *Phys. Rev. Lett.* 54, 2049 (1985).
42. H. F. Cheung and E. K. Riedel, *Phys. Rev. B* 40, 9498 (1989).
43. T. Brody, J. Flores, J. French, P. Mello, A. Pandey, and S. Wong, *Rev. Mod. Phys.* 53, 385 (1981).
44. H. Bouchiat, G. Montambaux, and D. Sigeti, *Phys. Rev. B* 44, 1682 (1991).

45. Y. Gefen, B. Reulet, and H. Bouchiat, *Phys. Rev. B* 46, 15922 (1992).
46. E. K. Riedel and F. von Oppen, *Phys. Rev. B* 47, 15449 (1993).
47. H. F. Cheung, E. K. Riedel, and Y. Gefen, 62, 587 (1989).
48. H. Bouchiat and G. Montambaux, *J. Phys. France* 50, 2695 (1989).
49. G. Montambaux, H. Bouchiat, D. Sigeti, and R. Friesner, *Phys. Rev. B* 42, 7647 (1990).
50. G. Montambaux, in "Quantum Fluctuations" (S. Reynaud, E. Giacobino, and J. Zinn-Justin, Eds.). Elsevier, Amsterdam, 1996.
51. C. P. Umbach, C. Van Haesendonck, R. B. Laibowitz, S. Washburn, and R. A. Webb, *Phys. Rev. Lett.* 56, 386 (1986).
52. B. Altshuler, Y. Gefen, and Y. Imry, *Phys. Rev. Lett.* 66, 88 (1991).
53. A. Schmid, *Phys. Rev. Lett.* 66, 80 (1991).
54. F. von Oppen and E. K. Riedel, *Phys. Rev. Lett.* 66, 84 (1991).
55. E. Akkermans, *Europhys. Lett.* 15, 709 (1991).
56. N. Argaman, Y. Imry, and U. Smilansky, *Phys. Rev. B* 47, 4440 (1993).
57. I. S. Gradshteyn and I. M. Ryzhik, "Table of Integrals, Series and Products." Academic, New York, 1965.
58. V. Ambegaokar and U. Eckern, *Phys. Rev. Lett.* 65, 381 (1990).
59. B. L. Altshuler, A. G. Aronov, and P. A. Lee, *Phys. Rev. Lett.* 44, 1288 (1980).
60. G. Montambaux, *J. Phys. I (France)* 6, 1 (1996).
61. A. Müller-Groeling, H. A. Weindenmüller, and C. Lewenkopf, *Europhys. Lett.* 22, 193 (1993).
62. G. Bouzerar, D. Poilblanc, and G. Montambaux, *Phys. Rev. B* 49, 8258 (1994).
63. M. Abraham and R. Berkovits, *Phys. Rev. Lett.* 70, 1509 (1993).
64. H. Kato and D. Yoshioka, *Phys. Rev. B* 50, 4943 (1994).
65. G. Bouzerar and D. Poilblanc, *Phys. Rev. B* 52, 10772 (1995).
66. M. Ramin, B. Reulet, and H. Bouchiat, *Phys. Rev. B* 50, 4943 (1994).
67. U. Eckern and A. Schmid, *Europhys. Lett.* 18, 457 (1992).
68. R. A. Smith and V. Ambegaokar, *Europhys. Lett.* 20, 161 (1992).
69. J. Clarke, W. M. Goubeau, and M. B. Ketchen, *J. Low Temp. Phys.* 25, 99 (1976).
70. C. Chapelier, M. E. Khatib, P. Perrier, A. Benoit, and D. Mailly, in "SQUID 91: Superconducting Devices and Their Applications" (H. Koch and H. Lubbig, Eds.). Springer, 1991.
71. L. P. Lévy, G. Dolan, J. Dunsmuir, and H. Bouchiat, *Phys. Rev. Lett.* 64, 2074 (1990).
72. R. Deblock, R. Bel, B. Reulet, H. Bouchiat, and D. Mailly, *Phys. Rev. Lett.* 89, 206803 (2002).
73. B. Reulet, M. Ramin, H. Bouchiat, and D. Mailly, *Phys. Rev. Lett.* 75, 124 (1995).
74. V. Chandrasekhar, R. A. Webb, M. J. Brandy, M. B. Ketchen, W. J. Gallagher, and A. Kleinsasser, *Phys. Rev. Lett.* 67, 3578 (1991).
75. D. Mailly, C. Chapelier, and A. Benoit, *Phys. Rev. Lett.* 70, 2020 (1993).
76. W. Rabaud, L. Saminadayar, C. Bäuerle, K. Hasselbach, A. Benoit, D. Mailly, and B. Etienne, in "Toward the Controllable Quantum States" (H. Takayanagi and J. Nitta, Eds.). 2003.
77. E. M. Q. Jariwala, P. Mohanty, M. B. Ketchen, and R. A. Webb, *Phys. Rev. Lett.* 86, 1594 (2000).
78. W. Rabaud, L. Saminadayar, D. Mailly, K. Hasselbach, A. Benoit, and B. Etienne, *Phys. Rev. Lett.* 86, 3124 (2001).
79. M. Pascaud and G. Montambaux, *Phys. Rev. Lett.* 82, 4512 (1999).
80. L. P. Levy, D. H. Reich, L. Pfeiffer, and K. West, 189, 204 (1993).
81. D. Ullmo, K. Richter, and R. A. Jalabert, *Phys. Rev. Lett.* 80, 4955 (1993).
82. Y. Noat, H. Bouchiat, B. Reulet, and D. Mailly, *Phys. Rev. Lett.* 80, 4955 (1998).
83. V. E. Kravtsov and V. I. Yudson, *Phys. Rev. Lett.* 70, 210 (1993).
84. V. E. Kravtsov and B. L. Altshuler, *Phys. Rev. Lett.* 84, 3394 (2000).
85. D. Goldhaber-Gordon, H. Shtrikman, D. Mahalu, D. Abusch-Magder, U. Meirav, and M. A. Kastner, *Nature* 391, 156 (1998).
86. V. Ferrari, G. Chiappe, E. V. Anda, and M. A. Davidovich, *Phys. Rev. Lett.* 82, 5088 (1999).
87. K. Kang and S. C. Shin, *Phys. Rev. Lett.* 85, 5619 (2000).
88. I. Affleck and P. Simon, *Phys. Rev. Lett.* 86, 2854 (2001).